Investigation of Device Dimensions on Electric Double Layer Microsupercapacitor Performance

By

Farheen Nasir

School of Chemical and Materials Engineering

National University of Sciences and Technology

February, 2019

Investigation of Device Dimensions on Electric Double Layer Microsupercapacitor Performance

Name: Farheen Nasir

Reg. No: NUST2016NSE04-00000170459

This thesis is submitted as a partial fulfillment of the requirements for the degree of

MS in Nanoscience and Engineering

Supervised by: Dr. Mohammad Ali Mohammad

School of Chemical and Materials Engineering (SCME)

National University of Sciences and Technology (NUST),

H-12 Islamabad, Pakistan

February, 2019.

DEDICATION

I dedicate my thesis to my parents, supervisor and instructors whose excellent examples have taught me to work hard for the things I aspire to achieve. I also dedicate it to my friends for their undying support and encouragement.

ACKNOWLEDGEMENTS

ABSTRACT

Electric Double Layer Capacitors (EDLC) are used in various energy storage applications such as hybrid vehicles, ultra fast charging smartphones and knitted electronics among other applications. They have also been used in combination with batteries to increase energy and power density. Extensive work has been done to understand the working mechanism of EDLC and effects of electrode and electrolyte material are well understood.

In this work we study the effects of EDLC design on capacitance of flexible laser scribed interdigitated microsupercapacitor (LSG-MSC). Three design parameters are tested to understand the effects of each on total capacitance. These parameters are: (1) current collector-electrode interaction, (2) electrode aperture and (3) distance between parallel electrodes. Detailed analysis was presented for the change in capacitance using cyclic voltammetry, electrochemical impedance spectroscopy and electrostatic simulation using COMSOL Multiphysics. It was found that in addition to electric double layer capacitance, there was also electric field being generated (i) between electrodes and (ii) between electrodes and current collector which lead to small electrostatic capacitance between them. This electric field was also found to cause disturbance in the double layer formation at the electrode thus causing change in the overall capacitance as the design parameters of the MSC were varied.

TABLE OF CONTENTS

<div style="text-align:right">Page No.</div>

LIST OF FIGURES

| | **DESCRIPTION** | **Page No.** |

LIST OF TABLES

LIST OF ABBREVIATIONS

	MEANING
AEC	Aluminum Electrolyte Capacitor
BSE	Backscattered Electrons
CCD	Cyclic Charge Discharge
CCG	Chemically Converted Graphene
CE	Counter Electrode
CNC	Carbon Nanocups
CNT	Carbon Nanotube
CRT	Cathode Ray Tube
CTE	Coefficient Of Thermal Expansion
CV	Cyclic Voltammetry
CVD	Chemical Vapor Deposition
EBL	Electron Beam Lithography
EDLC	Electric Double Layer Capacitor
EIS	Electrochemical Impedance Spectroscopy
ESR	Equivalent Series Resistance
FIB	Focused Ion Beam
FTIR	Fourier Transform Infrared Spectroscopy
GBL	γ-Butyrolactone
GO	Graphene Oxide
IBL	Ion Beam Lithography
LSG	Laser Scribed Graphene
MSC	Microsupercapacitors
MWCNT/MWNT	Multi Wall Carbon Nanotubes
NIL	Nanoimprint Lithography
PAE	Polyamine Ester
PAR	Polyarylates
PC	Polycarbonate
PEI	Polyetherimide

PEN	Polyethylene Naphthalate
PEO	Polyethylene Oxide
PES	Polyethersulphone
PET	Polyethylene Terephthalate
PI	Polyimide
PMMA	Polymethyl methacrylate
PVA	Polyvinyl Alcohol
PVDF	Polyvinylidene Fluoride
RE	Reference Electrode
rGO	Reduced Graphene Oxide
SBL	Scanning Beam Lithography
SE	Secondary Electrons
SEM	Scanning Electron Microscope
SMS	Surface Mountable Supercapacitors
SSG	Self-Stacked-Solvated-Graphene
TFT	Thin Film Transistor
THF	Tetrahydrofuran
WE	Working Electrode
XRD	X-Ray Diffraction

CHAPTER 1: INTRODUCTION

Over the past few decades the reliance on fossil fuels for energy has decreased sharply and now focus has shifted to other natural resources to fulfill our energy needs. Solar cells, wind turbines, hydropower, biomass etc. have emerged as green energy sources [1]. However, one of the biggest bottlenecks in the widespread commercialization of Green Energy Sources is the high cost of energy harvestation and storage [2]. Usually battery banks are used as energy storage devices but these are not ideal for use with Green Energy Sources because their lifetime is greatly affected by rapid power fluctuations caused by weather changes which is common during energy harvestation from Green Energy Sources [3, 4]. A new trend has developed towards using supercapacitors as energy storage [5-7]. There has also been extensive research on using battery-supercapacitor hybrids[8, 9]. Supercapacitors can withstand very high charge/discharge currents and have much longer lifetimes than batteries. They also allow the whole system to be much less heavy and thus have become an important area of research for energy storage with Green Energy Systems. Supercapacitors have also been commercially used in hybrid vehicles [10], ultra fast charging smartphones [11] and knitted electronics [12] among other applications. Companies such as Maxwell Technologies, AVX, Murata Electronics, Vishay, Nichicon and Cornell Dubilier are working on embedding supercapacitors into their products in order to increase their speed and improve lifetime. An emerging area of research for supercapacitors is wearable electronics. In this regard Levi's and Google partnered to release *Jacquard*, a smart jacket which can connect to the Internet, in September 2017. Although Jacquard is not the first commercial smart clothing venture, it is the biggest partnership seen so far. Other companies such as Ralph Lauren, Athos, Samsung, Polar and Owlet have introduced wearable electronics including smart shirts, sleeves, socks and even swimwear [13]. In 2015 Google filed a patent for a headband like device which would serve as a replacement for Google glass and sit on one side of the face [14].

1.1 FLEXIBLE ELECTRONICS

In the early 1960s, silicon wafers were thinned to ~100μm and assembled on plastic substrates to make flexible solar cells [15, 16]. This is termed as the start of flexible electronics. In the early 1980s Okaniwa *et al.* made p-i-n a-Si:G/ITO based solar cells on polymer substrates [17, 18]. In 1968 and 1969, Brody and colleagues developed the first Thin Film Transistor (TFT) on several substrates including paper, mylar and aluminum foil [19]. In 1994 polyimide was used for the first time to fabricate flexible a-Si:H TFT circuits by Constant *et al.* [20, 21]. In the early 2000s flexible displays, OLEDs and other commercial products started to become available. Flexible electronics has a wide range of applications including smart clothing, flexible solar cells, printed RFID, energy storage, printed sensors and OLED wallpapers [22]. In 2017 market analysis determined flexible electronics to be valued at USD 17.85 Billion. This amount is expected grow up to USD 40.37 Billion by 2023 [23]. While European countries are working on all aspects of flexible electronics (from materials to system and applications), USA has focused on military applications, whereas Asian countries have invested heavily on flexible displays and other consumer-based applications.

1.1.1 SUBSTRATES FOR FLEXIBLE ELECTRONICS

Flexible substrates act as a replacement for glass substrates and thus must have optical, mechanical, chemical, electrical, magnetic, surface and thermal properties that do not interact with the electronic circuits negatively. There are three types of substrates that are used for flexible electronics: (1) metals, (2) flexible glass and (3) organic polymers (plastic).

1.1.1.1. *Metals*

Metal substrates with less than ~125μm thickness are flexible and are attractive for systems which do not require transparent substrates. The most widely used metal for flexible electronics is stainless steel due to its high resistivity to corrosion and durability. Typical metal foils have inclusions as well as rolling marks which may result in device failure. Even the most cautiously rolled foils have average surface roughness of at least 100nm which is much higher than the <1nm for glass substrates. In order to improve electrical integrity of the devices, metal substrates must be polished [24] or planarized with a film [25].

Since metal contacts are electrically conductive, they must be coated with insulting layer to provide electrical isolations in circuits if needed. The insulating layer also acts as adhesive and as a barrier to chemicals. The insulating layer is usually 0.2-0.4μm.

1.1.1.2.   Flexible Glass

Glass plates are used commercially in flat panel displays. They can become flexible if its thickness is reduced to ~100μm [26]. Glass foils which are as thin as 30μm can also be produced which retain the advantage of plate glass such as optical transparency, low stress, high temperature tolerance, smooth surface with scratch resistance, low coefficient of thermal expansion, resistance to most chemical processes and electrical isolation among others. However, flexible glass is very fragile. In order to prevent breakage, it is often laminated with plastic foil or polymer coat.

1.1.1.3.   Organic Polymers

Polymer foils are flexible, allow roll-to-roll processing and are much cheaper than their counterparts. However, they require processing temperatures much less than glass and are prone to oxygen and water contamination. Modest coefficient of thermal expansion (CTE), dimensional stability and glass transition temperatures are important parameters to consider when selecting polymer substrate for any application. Polymer films are also prone to shrinking by heating and cooling cycles which can be prevented by prolonged annealing [27]. Organic polymers commonly used are divided into three categories:

  i.   Thermoplastic semi-crystalline polymer: examples include polyethylene naphthalate (PEN) and polyethylene terephthalate (PET).
 ii.   Thermoplastic non-crystalline polymer: examples include polyethersulphone (PES) and polycarbonate (PC)
iii.   High-Glass transition temperature materials: examples include polyarylates (PAR) and polyimide (PI).

PC, PAR and PES are transparent with high glass transition temperatures compared to PEN and PET but have high CTE and poor resistance to chemical processes. Thermoplastics such as PET and PEN as well as PI have comparatively small CTEs,

heightened elastic modulus and excellent resistance to most chemical processes thus being attractive candidates for flexible polymer substrates. Out of these three PI has the highest glass transition temperature but it is very sensitive to moisture in the atmosphere. This problem can be solved by insulation layer coating on PI.

Polyimide (PI)

Polyimide is made by polycondensation of aromatic anhydride with diamine in a polar solvent such as dimethylacetamide which forms polyamic acid. Soluble polyamic acid can then be made into fibre, impregnated fibrous reinforcements or films which are heated to convert them into PI. However, polyamic acid is highly unstable and must be stored in dry and cool conditions. Example of polyimide synthesis is shown in figure 1.1.
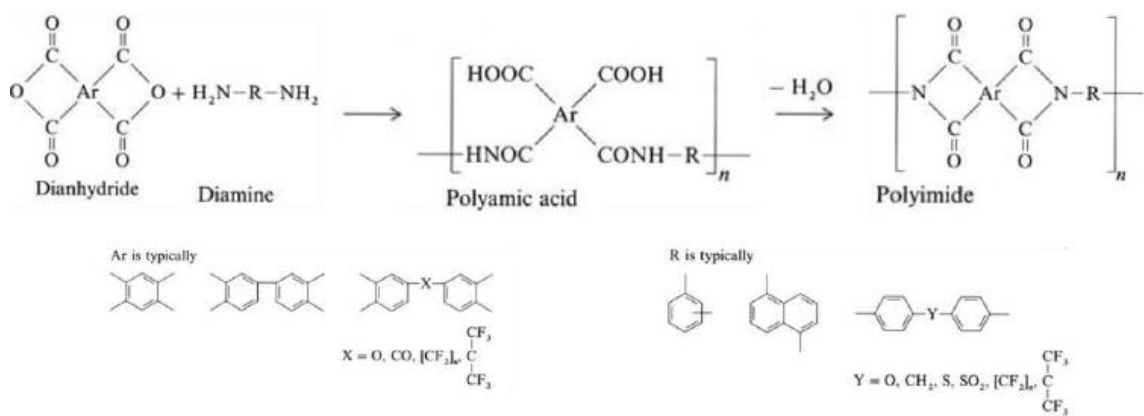
Figure 1.1: Synthesis of Polyimide using diacetylated diamines as the reactants [28]. Copyright 2006, IEEE. Reprinted with permission.

For the production of polyimide films and fibers, it is important that the polyamic acid be of very high molecular mass, stoichiometry and purity [29].

1.2 FABRICATION TECHNIQUES FOR FLEXIBLE ELECTRONICS

Flexible electronic devices are fabricated on very thin substrates which require special care in handling. Any variation in the curvature of the substrate during alignment process has the same effect as any misalignment during overlay of mask [27]. The

substrate may be temporarily bonded to a thick carrier, placed in tensioning frame or electrostatically or magnetically bonded to the carrier in order to prevent curving or cracking during processing. The adhesive between carrier and substrate must provide appropriate shear strength, resist processing chemicals, have small amount of degassing and release a small amount of contamination into the chamber. The adhesive must also be easily removable after processing. For example, although thermoplastic based adhesives provide the required resistance against most chemicals and can be easily removed by heating their maximum working temperature is often much lower than that of the substrate which makes the temperature window for processing much narrower which in turn can degrade device performance.

Fabrication process also offer constraints due to thermal limitation and radiation tolerances of polymeric materials. Bubbling, cracking or oxidation might occur in the polymer due to high temperature or radiation exposure during lithography. In addition, thermal expansion and thermal stress to the polymer chains are serious concerns that prevent usage of high energy procedures required for high-resolution structures. This has impeded the advancement of polymer based electronics devices despite the advantages in biocompatibility.

1.2.1. LITHOGRAPHY

Lithography refers to the process of transferring patterns and circuitry onto a substrate. These patterns are fed into a computer program or onto a mask and the writing is done using light, electron beam or ion beam.

1.2.1.1. *Photolithography*

Photolithography is the most commonly used technique for fabrication of electronic devices. It allows writing of multiple circuits at once (parallel writing) making it ideal for commercial use where throughput is an important factor. The first step in photolithography is the application of resist on the substrate. Next, metal mask with the required design is placed on the photoresist and UV light is shined to partially expose the resist to light. The resist material is such that it hardens (negative photoresist) or softens (positive photoresist) upon UV exposure. As a result the exposed area will be

stay on (negative resist) or wash away (positive resist) during development. Commonly used resists are Parylene C, SU-8 and Polyimide [30]. Figure 1.2 depicts common photolithography process.
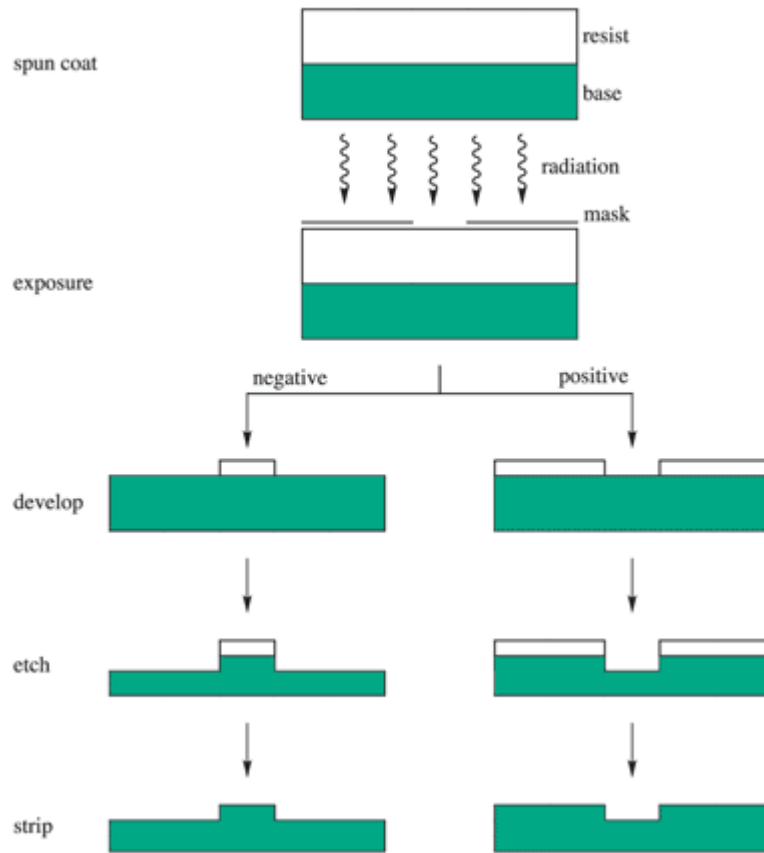
Figure 1.2: Photolithography for positive and negative tone resist and subsequent pattern transfer by etching. [31]. Copyright 1987, Blackie & Son Ltd. Reprinted with permission.

1.2.1.2. *Scanning Beam Lithography*

Scanning beam lithography is a direct writing technique which eliminates the need for patterned masks. A beam of electrons or ions is traced over the resist to produce chemical changes in it.

Electron Beam Lithography

Electron Beam Lithography (EBL) is a variant of Scanning beam lithography (SBL) which uses electron beam to induce changes in resist material. However, employing

EBL on polymer substrates is not without risk since the electron beam itself and the processing required for synthesis of EBL resist mask have the potential to damage polymer substrates. However, some research has been done to circumvent these obstacles and EBL has been successfully performed on polyethylene terephthalate by using a combination of metal coating and careful beam calibration for exposure dosage and energy [32, 33].

Ion Beam Lithography

Ion beam lithography (IBL) on polymers, uses focused ion beam (FIB) to pattern polymer materials. High energy Ga^+, He^+ or H^+ ions are used to penetrate the substrate. Very high aspect ratio features can be obtained from this technique because ion-electron interaction does not alter the ion trajectory [34].

1.2.2. ALTERNATIVE FABRICATION TECHNIQUES

Alternative patterning techniques such as nanoimprint lithography (NIL), nano cutting, self assembly and laser scribing have found success in fabrication of high resolution structures on polymer substrates. With imprinting techniques and self assembly, throughput as high as 10^4 m^2/h is easily attainable which is much higher than serial writing techniques such as EBL [35]. Some alternative techniques for polymer writing are shown in figure 1.3.
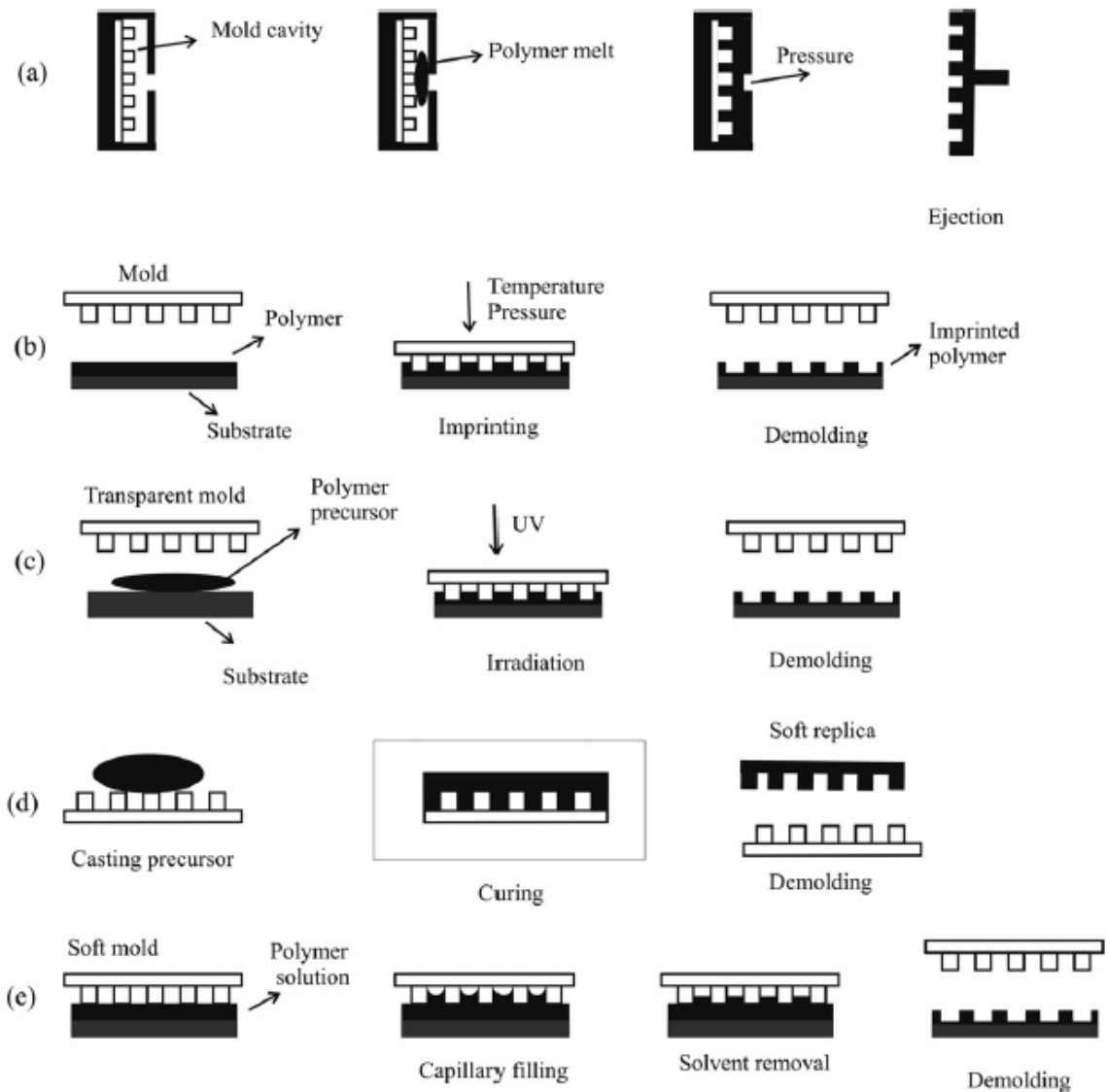
Figure 1.3: Alternative writing process. (a) Injection molding, (b) Nanoimprint lithography, (c) Ultra Violet Nanoimprint lithography, (d) soft lithography, (e) solvent assisted micromolding. [36]. Copyright 2008, American Chemical Society. Reprinted with permission.

Nanoimprint lithography

Nanoimprint lithography (NIL) is a flexible, low cost technique which is suitable for bioMEMS and other applications. It uses three components to achieve micrometer sized features on thin polymer film. Namely;

i.   Stamp with features fabricated on it (preferably by EBL and dry etching or by photolithography).

ii.   Polymer to be printed (having thickness of few nanometers, suitable molecular weight and glass transition temperature)

iii. Printing equipment (having temperature and pressure control of the substrate and stamp).

The stamp is pressed against the polymer with a pressure of 50-100 bar and the polymer is held at a certain temperature above its glass transition temperature [37]. The polymer flows to fill the gaps in surface topology of the stamp. Next, the stamp is removed and both substrate and stamp are cooled.

Laser Scribing

Laser scribing makes use of UV, Nd:YAG, excimer or pulsed laser to alter the surface chemistry of certain polymer materials. The materials commonly used for laser scribing are polyimide (PI), polyetherimide (PEI), polyethylene terephthalate (PET) etc. When laser strikes on the polymer, it changes its surface morphology by photothermal or photochemical reduction which causes materials such as nitrogen and oxygen to evaporate, leaving behind a conductive trace on the surface of an otherwise insulating polymer [38]. The process of laser scribing is shown in figure 1.4.
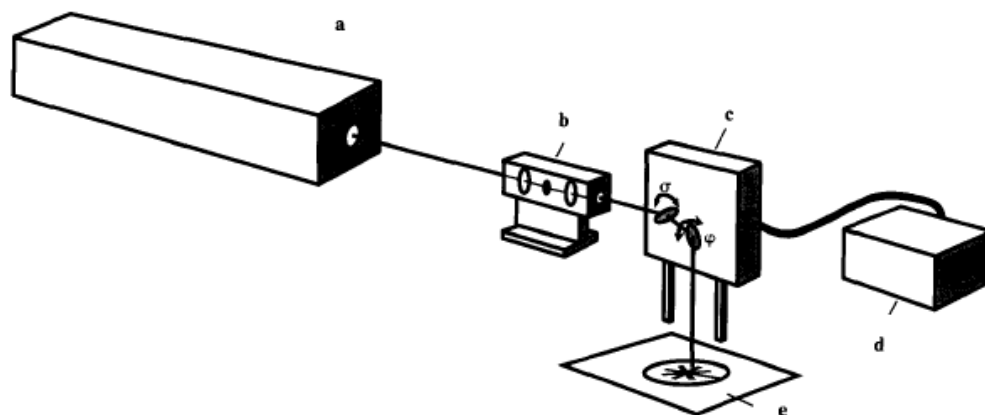
Figure 1.4: a) laser; b) focusing optics (optional); c-d) X-Y scanner with control; e) substrate [39].
Copyright 1994 Published by Elsevier B.V. Reprinted with permission.

1.3 SUPERCAPACITOR

Electrolytic capacitors store charge in the electric field between the two metal plates which are separated by a dielectric medium. For this reason, they can provide large bursts of energy very quickly but the amount of charge they can store is very small due to small surface area of the metal electrodes. Electrolytic capacitors thus have high power density but low energy density. On the other hand battery stores charge by chemical reaction. Since the chemical charging and discharging is a slow process, batteries can provide small amounts of energy for a relatively long time (greater energy density but smaller power density). Supercapacitors help bridge the gap between batteries and electrolytic capacitor. Due to their large surface area supercapacitors can store more charge than the conventional electrolytic capacitor allowing for greater energy density, and due to their charge storing mechanism they have at least 10 times greater power density than batteries and can withstand millions of charge and discharging cycles making them excellent for long term use. Supercapacitors are expected to reach market value of approximately USD 5.98 Billion by 2026 with Loxus, Panasonic, Maxwell, Nesscap, LS Mtron and Nippon currently being the major players. Current market reports indicate consumer electronics to be the most lucrative market for commercial supercapacitors with double layer supercapacitors expected to have significant shares in market over the next 8-10 years. Hybrid supercapacitors are expected to be close behind due to their exceptional power and energy densities as well as ability to withstand extreme temperatures [40].
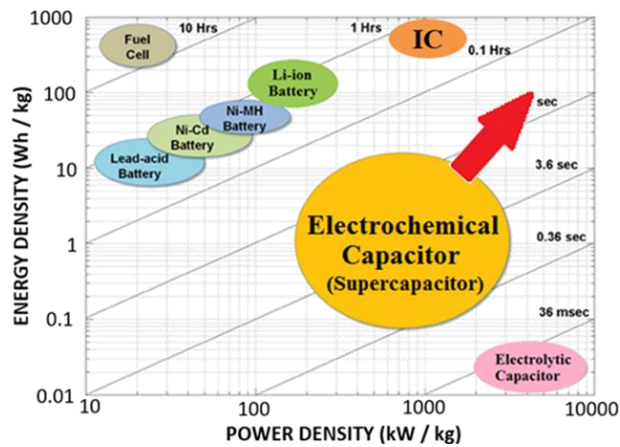
Figure 1.5: Energy vs. Power Density for energy storage devices.

Electrochemical capacitors (also called supercapacitors, aerogel capacitors or ultra-capacitors) are a type of energy storage device that uses two high surface area electrodes separated by an electrolyte. The electrolyte is a mixture of cations and anions in a solvent (for example; water). When potential is applied to the electrodes, ions from the electrolyte form a layer of opposite charge on surface of each electrode. These ions are physisorped on the surface of the electrode and the electric field generated between the charged electrode and the layer of counter ions gives rise to capacitance called *Electric Double Layer Capacitance (EDLC)*. These ions may also chemically interact with the electrode material giving rise to *Pseudocapacitance*. There is also a third type of electrochemical capacitor which utilizes both EDLC and Pseudocapacitance to store charge, called *Hybrid Supercapacitors*.

1.3.1   ELECTRIC DOUBLE LAYER CAPACITOR

The effect of double layer capacitance was described by Hermann von Helmholtz in 1853 [41]. In 1962 General Electric Company developed and patented the first electrochemical capacitor based on Helmholtz theory [42]. The early commercial supercapacitors were developed by Standard Oil of Ohio Research Center (SOHIO) and had porous graphite electrodes attached to current carrying conductors and used tetra-alkyl-ammonium (Al_2 $(SO_4)_3$) salt dissolved in a non aqueous solvent as electrolyte. These capacitors had capacitances ranging from 0.047 to 1F with Equivalent Series Resistance (ESR) values of a few ohms. The ESR values of these early supercapacitors were much higher than those commercially available today and so could only be used for applications which could withstand high ESR values. In early 1980s Matsushita Electric Industrial Company developed double layer capacitors with activated carbon woven into a fabric to serve as electrodes. This gave way to a new type of EDLC called Gold capacitors [43]. During the past two decades EDLCs have seen a surge in development and commercialization due to high demand from consumer electronics such as laptops, mobile phones and even electric vehicles. EDLC also have a much greater lifetime compared to batteries and are much more environmentally friendly making them an attractive alternative for clean energy systems.

1.3.1.1. Electric Double Layer Effect

The EDLC has the same energy storing principles as electrostatic capacitors i.e. larger plate area and smaller gap between plates give high capacitance. The difference is that while in electrostatic capacitors the plates are usually sheets of metal, in EDLC the plates are high surface area electrode and a layer of charged particles from the electrolyte adsorbed to its surface. The basic principle of electric double layer capacitance is shown in figure 1.6. When electric potential is provided to the high surface area electrodes, an electric charge is built up on them which attract oppositely charged particles from the electrolyte (co-ions). These co-ions are specifically adsorbed on electrode surface forming an immobile layer of ions near the surface called *Stern Layer.* This layer of co-ions in turn attracts solvated counter ions to from a loosely bonded second layer of ions. In EDLC, solvent molecules separate the electrode and the layer co-ions effectively behaving as a molecular dielectric. In this case there, is no charge transfer occurring between the electrode and the ions from the electrolyte so the adsorption is purely based on physical forces such as electrostatic force. The distance between electrode and layer of co-ions is a few Angstroms thus the capacitance achieved is much higher than that for electrolytic capacitors. The adsorption process is shown in figure 1.7.
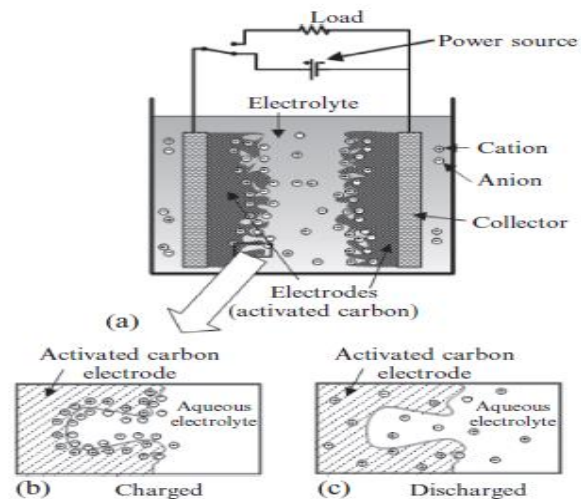
Figure 1.6: Double layer capacitance formed at two electrodes. (a) Practical EDLC (b) Charged conditions (c) discharged conditions [44]. Copyright 1994 Published by Elsevier B.V. Reprinted with permission.
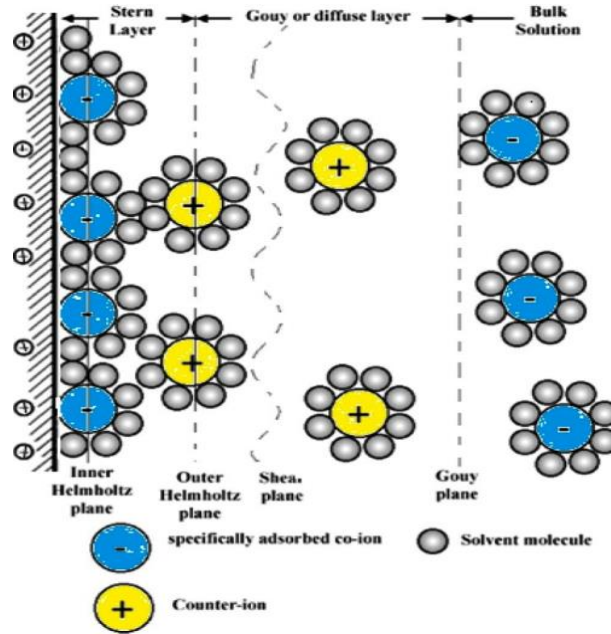
Figure 1.7: Charge adsorption on electrode surface[45].Reprinted with permission.

1.3.1.2. Modeling of EDLC

As mentioned before, Hermann von Helmholtz presented the idea of electric double layer capacitance. He stated in his double layer model that for a charged electrode in an electrolytic solution, another electrode is formed the electrode/electrolyte interface by ions from the electrolyte solution and the two electrodes are separated by a distance of a few Angstroms. This is shown in figure 1.8 (a). This double layer is considered to be a molecular capacitor with distance between the plates in Angstroms thus having very high specific capacitances. However, this model is only valid for solutions with very high electrolyte concentration.

In 1910 and 1913 respectively, Guoy and Chapman gave separate theories for electric double layer formation in dilute solutions [46, 47]. The combination of their respective explanations became known as the Gouy-Chapman model. In the combined model, exchange of counter ions between stern layer and the bulk of the solution is also considered. The effect of thermal motion and coulomb forces on counter ion distribution is also described, as shown in figure 1.8 (b).

In 1923, Stern described two regions of ion distribution using Helmholtz and Gouy-Chapman models. The inner region, which was initially described by Helmholtz, is called the compact/Stern layer and the diffused ions which form a loose layer in the outer region are called Gouy-Chapman layer. This is shown in figure 1.8 (c). The two regions are also called inner Helmholtz plane (IHP) and outer Helmholtz plane (OHP). Total capacitance C_{dl} for the EDLC is considered to be a combined effect of capacitances from IHP (Stern layer capacitance C_s) and OHP (capacitance due to diffusion layer C_{diff}).

$$\frac{1}{C_{dl}} = \frac{1}{C_S} + \frac{1}{C_{diff}}$$

The practical EDLC has a high surface area porous electrode and the electric double layer behavior is affected by several parameters including space constraints of the pores, electrolyte resistance, mass transfer path and wettability of porous electrode, thus it cannot be fully described by the models shown in figure 1.8.
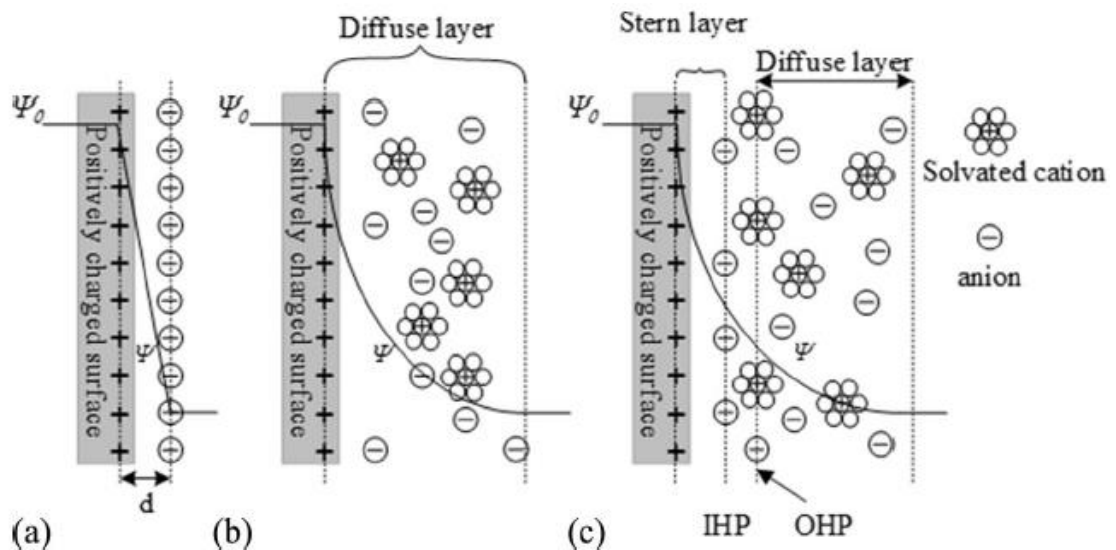
Figure 1.8: Double layer models by: (a) Helmholtz, (b) Gouy-Chapman and (c) Stern [44]. Copyright 1994 Published by Elsevier B.V. Reprinted with permission.

Practical EDLC and its equivalent circuit are shown in figure 1.9. The total capacitance of each electrode is defined as:

$$C_{dl} = C + = C - = \frac{\varepsilon_0 \varepsilon_r}{d} A$$

Where, ε_0 and ε_r are the dielectric constants of vacuum and electrolyte respectively, d is electric double layer width (Debye length) and A is electrode surface area. The total capacitance of the system (C_t) is then:

$$\frac{1}{C_t} = \frac{1}{C_+} + \frac{1}{C_-}$$

However, experimental results indicate that the complete behavior of EDLC cannot be described by the above equations [48].
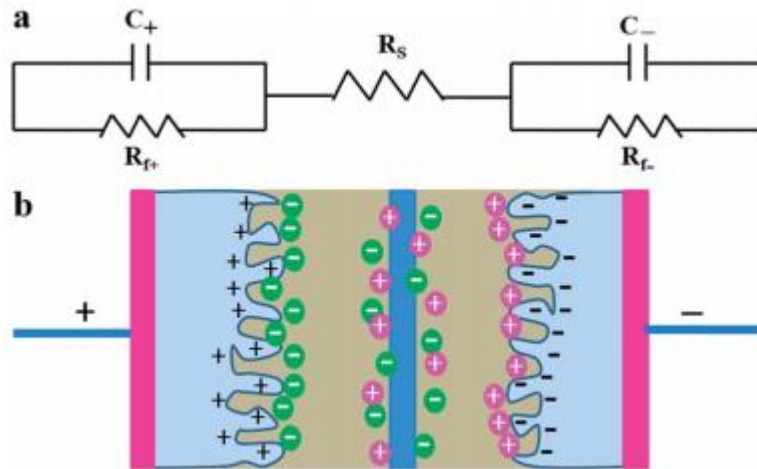
Figure 1.9: (a) Equivalent circuit model for EDLC (b) schematic for practical EDLC [49]. Copyright 2014, American Chemical Society. Reprinted with permission.

1.3.1.3. Electrode Materials

The main requirement for high capacitance is to have a material with exceptionally high surface area with good electrical conductivity. For this reason there are three different types of materials used in EDLC namely, carbon, conductive polymers and metal oxides.

Carbon

Carbon is useful in all types of electronic devices due to its chemical stability, processing feasibility and wide operating temperature range. In order to improve the available supercapacitors, many carbon materials with high porosity have been

developed over the years such as activated carbon, graphene, carbon nanotubes (CNT), carbon aerogels and carbon onions to name a few.

Amongst the carbon/carbon supercapacitors, Activated Carbon is the most commonly used. It consists of highly porous carbon produced by heating petroleum coke, coal or pitch. The inner surface of an electrode fabricated by activated carbon is padded with porous carbon which increases its surface area by 100,000 times that of ordinary electrolytic capacitor. However, decrease in availability of fossil fuels and heightened awareness about the environmental effects of these materials has pushed researchers to find better alternatives for the production of activated carbon. Materials such as wood, cellulose and sugar canes have emerged as possible raw materials for activated carbon though they have significantly lower yield than fossil fuels. It is likely that these renewable energy sources will dominate the future market for activated carbon production. Table 1.1 shows the raw material cost and carbon yield for different materials.

Table 1.1: Raw material cost and corresponding carbon yield by pyrolysis for activated carbon[50]. Copyright 2012 Elsevier Ltd. Reprinted with permission.

Raw material	US$ cost (kg)	Carbon yield (percentage by weight)
Petroleum coke	1.4	90
Charcoal	1.2	90
Lignite	0.75	50
Coconut shell	0.25	30
Wood	0.8	25
Potato starch	1.0	45
Sucrose	0.25	<45
Cellulose	0.65	<45
Corn grain	0.25	<45
Banana fiber	4	<45

Another commonly used material for supercapacitors is Graphene. It is a 2D layer of carbon atoms. Since its discovery in 2004 [51] Graphene has garnered a lot of attention due to its excellent properties. The first graphene based supercapacitors were developed in 2011 by Miller *et al.* [52]. Graphene can be synthesized by several methods including Chemical Vapor Deposition (CVD), nanotube slicing, Langmuir-Blodgett, spin coating, carbon dioxide reduction and laser scribing among others.

Large ESR is a major parameter that needs to be considered when selecting material for supercapacitor. Large ESR values are mostly caused by resistance in the electrodes, the bulk phase electrolyte and from ion migration into the porous structure. Carbon Nanotubes have been shown to improve electrode conductivity and thus increase capacitance due to their high electrical conductivity and ability to form porous structure [53].

Conducting Polymers

Polypyrrole, polythiophene, polyaniline etc. are commonly used conducting polymers for supercapacitor applications. The charge storing mechanism for these materials is mainly faradaic reactions however they have exceptionally porous structure making them suitable for double layer capacitors. Conducting polymers are only capable of storing charge once doped but have very high conductivity when charged along with fast charge/discharge rates, making them good candidates for low equivalent series resistance, high energy and power density devices. The highest specific capacitance using conducting polymers was achieved by n and p doped thiophene based polymers to fabricate negative and positive electrodes respectively. The specific capacitance was measured to be 95-220F/g for p-doped electrode and 80-165 F/g for n-doped electrode [54].

Metal Oxide

Oxides of transition metals such as Ni, Cu, Ru, Fe and Mn have been widely used for electrode materials in order to combine the effects of electric double layer capacitance and pseudocapacitance. RuO_2 is the most widely used material for this purpose however its cost and toxicity has forced researchers to look for other alternatives. CuO and TiO_2 have become attractive due to their high capacitance, environmental friendliness, high abundance and safety among other reasons [55, 56].

1.3.1.4. Electrolyte

EDLCs have been fabricated with different kinds of electrolytes. The electrolytes are typically differentiated into three categories i) Organic electrolyte, ii) Aqueous, and iii) Ionic liquids.

Aqueous Electrolyte

Aqueous electrolytes have an operational voltage of around 0.6-1 V but their low cost and high ionic conductivity make them appealing for several low power applications. The major disadvantage of aqueous electrolyte is their corrosion of supercapacitor electrodes at higher voltage and temperature which decreases the lifetime of supercapacitors.

Organic Electrolyte

Currently most commercial supercapacitors used organic electrolytes. They have life cycles beyond 1 million cycles; can operate on moderately high voltages of around 2.2-2.9V and have operating temperature between -30 to 50°C. However, they are prone to flammable since organic solvents have very high vapor pressure. Organic solvents provide excellent potential window but their high flammability, toxicity and low thermal stability prevent their usage in high performance applications.

Ionic Liquids

Ionic liquids consist entirely of cations and anions and are molten salts at room temperature. The cations limit the negative potential window while anions influence positive potential and working temperature range for the supercapacitor. Ionic liquids have low vapor pressure, good conductivity above 60°C, high voltage stability (up to 4V) and high thermal stability which make them suitable for several applications such as electric vehicles, hybrid engines, mobile phones etc. Additionally these electrolytes are non-toxic, non-flammable and non-volatile. However, lower ionic conductivity and much high costs have prevented ionic liquids from becoming the go-to electrolyte for commercial applications.

1.3.2   PSEUDOCAPACITOR

Pseudocapacitors were first developed in 1997 by Conway *et al.* [57]. In these types of capacitors reversible redox reactions usually occur, which give rise to pseudocapacitance due to Faradaic currents from reactions and resulting charge transfer. The value of pseudocapacitance is voltage dependent but advances have been made to use metal oxide-based pseudocapacitors to maintain constant capacitance with fluctuating voltage [58]. While EDLCs have specific capacitance between 20 to $50mF/cm^2$, pseudocapacitors can have specific capacitance as high as $500mF/cm^2$. Some of the processes associated with pseudocapacitors are:

i)   Two dimensional deposition of adatom array on the surface of electrodes.

ii)   Redox process in electrolyte solution.

iii)   Chemisorptions of ions on the electrode surface.

1.3.3   HYBRID CAPACITOR

In a hybrid capacitor, one of the electrodes stores charge electrostatically (electric double layer formation) while the second one stores charge faradaically (pseudocapacitive behavior). The most popular materials for hybrid capacitors are porous tantalum for anode (double layer capacitor) and ruthenium oxide for cathode where redox reactions take place. Hybrid capacitors have operational voltage up to 125 V and temperature range between -55 to 200°C. Given that hybrid capacitors consist of series connection between two different types of capacitors, the total capacitance is found by $\frac{1}{Ct} = \frac{1}{Cc} + \frac{1}{Ca}$ where C_t is the total capacitance of the hybrid capacitor, C_c is the capacitance of the pseudocapacitive cathode and C_a is double layer capacitance on anode. We know that pseudocapacitance is much larger than double layer capacitance ($C_c \gg C_a$), so C_t is close to C_a. The capacitance and ESR of hybrid capacitor are heavily dependent on temperature and ESR at low temperature can be several times higher than that at room temperature. However, the energy density of the hybrid capacitor is much higher than that for a double layer capacitor for the same power density. Since the materials used for hybrid capacitors are very expensive, they can only be used in devices where the need of performance justifies the cost.

CHAPTER 2: LITERATURE REVIEW

2.1 FLEXIBLE SUPERCAPACITORS

Rapid growth in portable electronics market has sped up the development of high performing, flexible and reliable energy storage devices [59, 60]. Flexible supercapacitors have garnered a lot of interest in recent years due to their high energy density, small size, light weight, flexibility, ease of handle and large temperature window [61-64]. Studies on their development has focused mainly on liquid based supercapacitors with liquid based electrolytes [65, 66]. However, liquid electrolyte based supercapacitors are not suitable for portable electronics due to their high cost, leakage and toxic and corrosive behavior of electrolytes [67]. Recently there has been a shift towards solid state supercapacitors due to their many advantages including low packaging cost since solid state electrolytes do not pose the risk of leakage as well as wider operating temperature range and ease of handling. [68-74]. Significant amount of work has been done to create flexible electrodes with high energy density. Carbon-based electrodes have been the most extensively studies class of electrode material for flexible supercapacitors [70, 73-77] due to their excellent conductivity, cyclic stability, power density and outstanding mechanical properties as well as no need for separate current collectors or binders [78-82]. Another important parameter affecting the rate capability of supercapacitor is the electrolyte. Solid state electrolytes offer high rate capability and stability compared to other types of electrolytes. Gel polymer electrolytes are amongst the most extensively researched solid state electrolytes due to their high ionic conductivity [71, 83-86].

2.1.1. FLEXIBLE ELECTRODES

Flexible, robust and high electrochemical performance supercapacitors still remain a challenge to fabricate. Previously, flexible electrodes have been developed on Ti and Ni foils [87-89] as well as stainless steel grids [90, 91] however these have not been successful since they are easily corroded in aqueous electrolytes. These metal foils are also less flexible and weigh much more than plastic substrates thus negatively effecting

power and energy densities of the supercapacitor. Recent trend has been to move away from metal to non-metal substrates.

In this regard carbon based electrodes on flexible, light weight and porous substrates have been very popular [62, 72, 77, 79, 81, 84, 92-94]. In 2010 Hu *el al.* fabricated flexible electrodes by using paper as a substrate with CNT absorbed into it [92]. A uniform layer of CNT was coated on the substrate using capillary effect. The sheet resistance achieved by this process was 10Ω/sq. and the fabricated supercapacitor exhibited extraordinary capacitance of 200F/g at 1A/g. Later in 2011 Zheng *et al.* used the same idea to coat multilayer graphene on cellulose paper to create graphene paper with specific capacitance up to 2.3mF/cm^2 [93]. Hu *et al.* also synthesized CNT-cotton electrode by dipping and drying method [95]. The supercapacitors fabricated by these electrodes were able to achieve specific capacitance of 0.48 F/cm^2 and areal energy density 20Wh/kg at specific power 10kW/kg. CNTs have also been prepared directly on paper by vacuum filtration [96] or by CVD [97, 98]. These paper based CNTs were directly used as electrodes for supercapacitors and were able to deliver high power density of >100kW/kg.

Graphene has been shown to have greater surface area than CNTs and stronger inter sheet Vander Waal forces. However, restacking of graphene sheets greatly decreases the available surface area for double layer capacitance [99]. Several experiments have been done to resolve the restacking issue of graphene [100-102]. Yang *el al.* discovered that chemically converted graphene (CCG) sheets when hydrated remained neatly separated [101]. Based on this method they produced thin films of wet self-stacked-solvated-graphene (SSG) with CCG in very small amount (approximately 0.45 mg/cm^2). Supercapacitors fabricated by wet SSG films were able to achieve specific capacitance as high as 215 F/g. This capacitance is much greater than that for thermally annealed and freeze dried SSG electrodes. They concluded that the incredibly high specific capacitance of wet SSG is due to its very fast ion diffusion and high surface area. Lu *et al.* used multiwall CNTs to form CNT-graphene composite electrodes [102]. These electrodes were highly porous since CNTs acted as separator by increasing the basal spacing thus enhancing the electrolyte transportation deep into the electrode.

Remarkable 256 F/g specific capacitance was obtained for the fabricated supercapacitors.

In 2012 Strong *et al.* demonstrated an inexpensive way to make graphene on flexible materials [103]. They used 788nm laser to reduce graphite thin films into conductive laser scribed graphene (LSG). Later Kady *et al.* developed microsupercapacitor (MSC) on flexible polyethylene terephthalate (PET) substrate using the same laser scribing technology. They were able to fabricate more than 100 microsupercapacitors on a single disc in less than 30 minutes with volumetric power density of 200W/cm^3 as shown in figure. 2.1 [104]. It was also discovered that heteroatom can easily be doped into the carbonaceous structure of LSG in order to increase current density and conductivity as well as to improve pseudocapacitance and electrolyte wettability of the substrate. Boron doped LSG MSC was fabricated by Peng *et al.* which achieved specific capacitance of 16.5mF/cm^2 which was three times higher than that for undoped MSCs. LSG has also been used as scaffold for depositing pseudocapacitive materials due to its porous 3D structure. MnO_2 was electrochemically deposited on LSG electrode to form hybrid electrode for MSC [105]. The fabricated device showed capacitance of 400 F/cm^2 and had energy density of 35.6μWh/cm^2.

Some metal oxides and conducting polymers have also been used as substrates for pseudocapacitors such as TiO_2 [106, 107] ZnO [108, 109], Zn_2SnO_4 [110], WO_x [74], PANI [111], PPy [112], PEDOT [113] etc. For example Bao *et al.* developed electrochemical capacitors by coating MnO_2 on Zn_2SnO_4 nanowires and using carbon microfibers as substrate [110]. They obtained ultra high capacitance of 621.6F/g with aqueous Na_2SO_4 as electrolyte. Lu *et al.* created flexible hybrid $WO_{3-x}@Au@MnO_2$ electrode having ultra high capacitance of 1195 F/g [74].
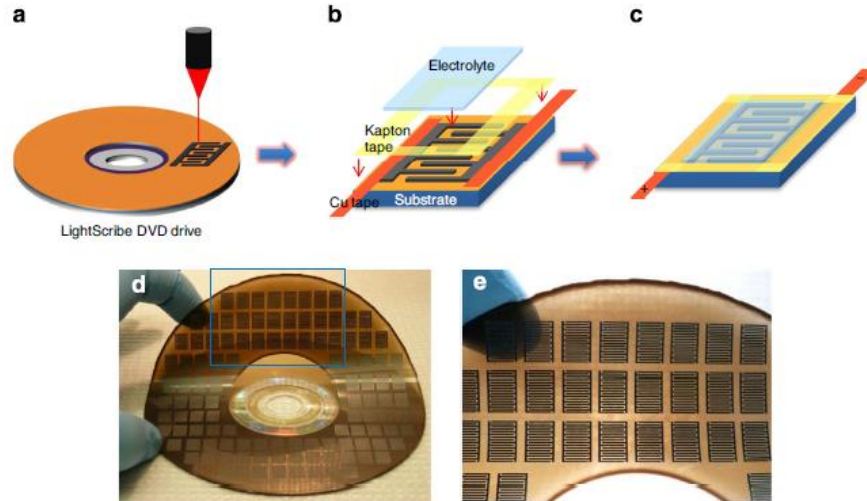
Figure 2.1: (a-c) steps for the fabrication of LSG MSC on PET supported GO film. (d-e) More than 100 MSC can be fabricated on a single disc in one run [104]. Copyright 2013, Springer Nature. Reprinted with permission.

2.1.2.   GEL POLYMER ELECTROLYTE

Solid state supercapacitors require solid electrolytes having good reliability and wide operating temperature range. They are also easier to handle compared to their liquid counterparts. The most commonly used electrolyte in solid state supercapacitors is gel polymer electrolytes which is non toxic and has very high ionic conductivity even at room temperature (10^{-3} – 10^{-4} S/cm). These electrolytes consist of polymeric host framework, plasticizer (mixture of two or more aqueous or organic solvents) and an electrolytic salt. Polyvinyl alcohol (PVA) [68, 85], polyvinylidene fluoride(PVDF), polyethylene oxide (PEO) [114], polyamine ester (PAE) [86] and polymethyl methacrylate (PMMA) [113] are some examples of host polymers. The most widely used organic solvents for high conductivity, low viscosity plasticizer with wide potential window are propylene carbonate (PC), γ butyrolactone (GBL) and tetrahydrofuran (THF) [83, 86, 113].

Solid state electrolytes are categorized according to type of electrolytic salt used. The salt in gel polymer electrolyte should have large number of ions with very low dissociation energy.

2.1.2.1. Lithium Ion Gel Electrolyte

Various lithium ion gels have been used in electrolytes for batteries and supercapacitors over the years. They are prepared by mixing lithium salt and polymer in organic solvent between 70-170°C. Huang *et al.* synthesized a gel polymer electrolyte with large potential window and excellent ionic conductivity ($6.9x10^{-3}$ S/cm) using polyethylene glycol blending polyacrylonitrile as polymeric host, $LiClO_4$ as salt and dimethyl formamide as plasticizer [83]. In 2012 Wang *et al.* used PVA host with LiCl salt and water as a solvent [71]. This mixture prevented irreversible oxidation reaction at the electrode and was able to maintain mechanical stability of the electrode during charge discharge cycles. For example, VO_x and VN electrodes showed impeccable capacitance retention without sacrificing their performance [115].

2.1.2.2. Proton Conducting Ion Gel Electrolyte

Given that proton (H^+) has much higher mobility than Li^+ it is a significantly better candidate for ultrafast supercapacitors. Electrolytes containing protons are prepared by adding polymer matrix to a polar solvent with proton donors such as H_2SO_4 and H_3PO_4. Most commonly used proton conducting gel electrolyte are PVA/ H_3PO_4 [74], PVA/ H_2SO_4 [68, 85]and PVA/ $H_3PO_4/H_4(W_{12}SiO_{40})$ [116] each having conductivity between 10^{-4} to 10^{-2} S/cm at ambient conditions. Lian *et al.* created PVA/ $H_3PO_4/H_4 (W_{12}SiO_{40})$ electrolyte and the subsequent supercapacitors made with the electrolyte sandwiched between graphite electrodes was able to withstand ultrahigh charge discharge rates of 20V/s. They also cross linked $H_4(W_{12}SiO_{40})$ with PVA to synthesize a new gel electrolyte having rate capability of 50V/s [117]. Q Chen *et al.* studied the electrolytic performance of different acids in proton conducting gel electrolytes using PET substrate with conductive graphene film used as electrodes [118]. They found that PVA/ H_3PO_4 based electrolyte gave significantly better performance than PVA/ H_2SO_4 and PVA/NaOH due to its high ionization.

2.1.2.3. Alkaline Gel Electrolytes

Alkaline gel electrolytes have great potential in alkaline batteries and supercapacitors [119-121]. Electrolytes such as P(ECH-co-EO)/KOH/H_2O [119], PAAK/ KOH/H_2O [122], PVA/KOH/H_2O [121] and PEO/KOH/H_2O [120] have been extensively

researched. Lewandowski *et al*. modulated the ratio of all three components in PEO/KOH/H_2O electrolyte and were able control the ionic conductivity of the electrolyte which reached up to 10^{-3} S/cm [120]. Yang *et al.* synthesized PVA/KOH/H_2O electrolyte with ultra high ionic conductivity of 10^{-2} S/cm [121, 123]. Li *et al.* utilized femtolaser to create reduced graphene oxide (rGO) and simultaneously doping it with $HAuCl_4$ nanocomposite to create gold electrodes [124]. The fabricated supercapacitor had 100 times higher electrode conductivity than conventional supercapacitors thus providing significantly higher rate capability and specific capacitance. Table 2.1 shows the electrochemical performance for different capacitors.

Table 2.1: Electrochemical performance of various capacitors.

Electrode Material	Electrolyte	Capacitance	Power Density	Energy Density	Cyclic Stability	Ref.
VS_2 MSC	$BMIMBF_4$/ PVA	4.7Mf/cm^2 at 100mA/cm^2	-	-	100% retention after 1000 cycles	[125]
rGO/Au nanoparticle MSC	H_2SO_4/PVA gel	0.77mF/cm^2 at 1V/s	-	-	99% retention after 10,000 cycles	[124]
rGO	H_2SO_4/ solvent-cast Nafion electrolyte membranes	118.5F/g at 1A/g	-	-	100% retention after 1000 cycles	[126]
LSG MSC	H_3PO_4/PVA gel	0.8mF/cm^2 at 10mV/s	-	-	96% retention after 3000 cycles	[127]

rGO MSC	Hydrated GO	0.51 mF/cm^2 at 40mV/s	1.7 W/cm^3	43 mWh/cm^3	80% retention after 4000 cycles	[128]
Graphite	SiWA/H$_3$PO$_4$ /PVA	1mF/cm^2 at 1V/s	-	-	-	[116]
Boron doped LSG	H$_2$SO$_4$/PVA gel	3 mF/cm^2 at 40mA/cm^2	-	0.56 mWh/cm^3	90% retention after 12000 cycles	[129]
CNT/PANI	H$_3$PO$_4$/PVA gel	16F/g T 0.16 mA/cm^2	-	-	50% retention after 200 cycles	[130]
LSG MSC	H$_2$SO$_4$/PVA gel	2.32 mF/cm^2 at 16.8mA/cm^3	200 W/cm^3	-	96% retention after 10000 cycles	[104]

2.1.3.   GENERATIONS OF SUPERCAPACITORS

Supercapacitors are categorized into different generations in terms of electrode material, type of electrolyte and design. In this section we describe the various generations of supercapacitors with respect to their designs and analyze the performance of each generation.

2.1.3.1.   *Sandwiched Geometry*

Sandwiched supercapacitor, also known as stacked supercapacitor, is the simplest design for supercapacitor applications. Two electrodes are placed on top of each other and separated by a layer of electrolyte as well as a separator to prevent short circuit in case of electrolyte breakdown. Figure 2.2 shows the structure of stacked supercapacitor. Jung *et al.* fabricated stacked supercapacitor by using branched graphite films (called carbon nanocups, CNC) to increase the available surface area [131]. They achieved specific

capacitance up to 407μF/cm^2 for CNC electrodes which was 5.3 times higher than that for concave supercapacitors with no extended surface area. The biggest disadvantage of stacked geometry is that due to its height (z-axis dimension), it cannot be used for in-plane energy storage as required by wearable electronics and other such applications. However, it remains very popular in testing the storage capability of electrode materials and electrolytes since it does not require complex fabrication techniques that other geometries do [105, 132-136].
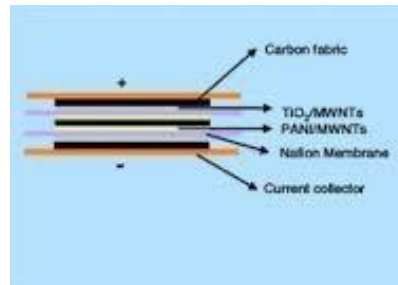
Figure 2.2: Stacked supercapacitor [137]. Reprinted with permission.

2.1.3.2.   In-plane Geometry

There are several different types of in-plane geometries which not only allow for easy integration of supercapacitor with other devices but also increase the total surface area accessible to the electrolyte thus increasing specific and volumetric capacitance as well as device energy density. Some of the most commonly used in-plane geometries are described below. However, this list is not exhaustive as there can be several different geometries which can be used to enhance the surface area of the supercapacitor as well as for appealing designs in wearable electronics.

Interdigitated Microsupercapacitor

Interdigitated Microsupercapacitors (MSC) are the most commonly used geometry for commercial supercapacitors. It consists of two comb shaped electrodes separated by an electrolyte (figure 2.3). The combed geometry allows two electrodes to be in the same plane and significantly increases the surface area compared to sandwiched structures. Interdigitated MSCs can be fabricated by various lithography techniques as well as laser scribing and molding. Gao *et al.* fabricated supercapacitors with various geometries using laser scribing [128]. They found that the energy storage for interdigitated MSC

was higher than that for any other geometry. Kim *et al.* designed interdigitated MSC using Multi Wall Carbon Nanotubes (MWCNT) as flexible electrodes [138]. As they varied the in-plane dimensions of the MSC they found a change in capacitance which they ascribed was due to change in ion diffusion pathway. Ferris *et al.* designed 3D MSCs with hydrated RuO_2 electrodes on gold current collectors in order to achieve energy density comparable to lithium ion batteries but having greater power density and cyclic stability than conventional batteries [139]. Xie *et al.* conducted performance test on state-of-the-art surface mountable supercapacitors (SMS), aluminum electrolyte capacitor (AEC) and laser scribed graphene (LSG) based microsupercapacitor (MSC) [140]. They found that even though the operating voltage for AEC was higher than SMS and MSC, its capacitance was significantly lower. LSG MSC exhibited 3.75 times higher capacitance than commercial SMS and 8785 times higher than AEC.
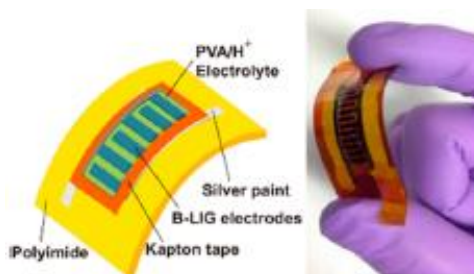
Figure 2.3: Interdigitated Microsupercapacitor [129]. Copyright 2015, American Chemical Society. Reprinted with permission.

Concentric Circular Microsupercapacitor

Concentric supercapacitors are shown in figure 2.4. They possess larger surface area than stacked supercapacitors but less than that for microsupercapacitors. Wang *et al.* fabricated concentric microsupercapacitors on PET substrate by using laser scribing [141]. The fabricated supercapacitor exhibited high areal capacitance and flexibility. The capacitance was noticeably increased with bending which was possibly due to decrease in space between the electrodes and excellent flexibility of the supercapacitor. Li *et al.* utilized polypyrrole based concentric circular MSC in combination with MWCNT/PANI ethanol gas sensor to fabricate wearable gas sensor for easy, fast and reliable testing equipment for drunk driving [142].
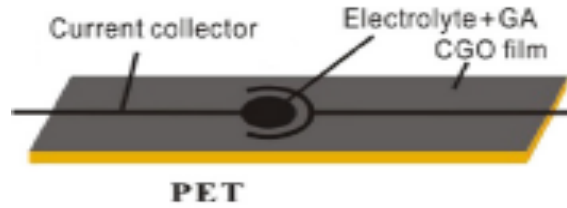
Figure 2.4: Concentric Circular Microsupercapacitor [141].Copyright 2017 Elsevier B.V. Reprinted with permission.

Fractal Microsupercapacitor

Hota *et al.* designed fractal microsupercapacitors in 2017 to show that the specific capacitance for the fractal design is significantly higher than that for interdigitated MSCs [143]. They found that 16% increase in surface area for fractal design corresponds to 32% increase in capacitance when compared to interdigitated design. They attributed this non-linear increase in capacitance due to additional capacitance caused by edging electric field at the electrode edges of fractal MSCs. Several fractal designs implemented by Hota *et al.* are shown in figure 2.5 as well as fabricated interdigitated MSC for comparison.
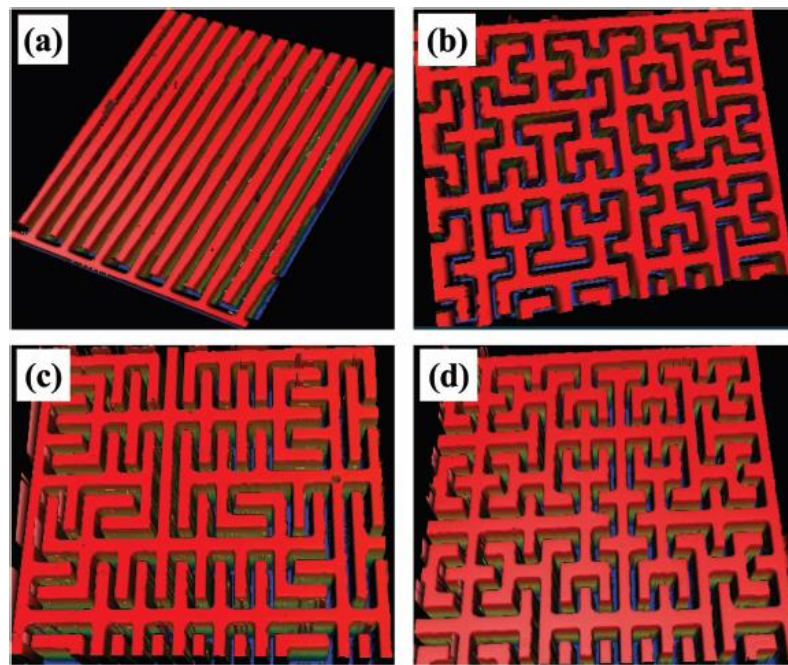
Figure 2.5: a) Interdigitated MSC; b) Fractal Hilbert MSC; c) Peano MSC; d) Fractal Moore MSC [143].Copyright John Wiley and Sons. Reprinted with permission.

2.2 Laser Scribing

Laser scribing on flexible substrates was introduced in 2011 when Gao *et al.* demonstrated fabrication of microsupercapacitor directly on hydrated graphite oxide films [128]. Since then different materials have been used to directly pattern conductive paths onto otherwise insulating materials. Most commonly used materials for laser scribing are graphene oxide (GO) [144-146], polyimide (PI) [127, 129], polyethersulfone (PES) [147], and polyetherimide (PEI) [148]. Other materials such as paper [149], wood [150], bread and other edible items [151] have also been tested to check formation of graphene as a result of laser scribing. As mentioned in chapter 1 high energy laser irradiation converts the surface of an organic material into conductive graphene by breaking chemical bonds and eliminating materials such as hydrogen, oxygen and nitrogen. The resulting laser scribed graphene (LSG) has high conductivity as well as very high porosity which increase its surface area making it an ideal candidate for use in high energy density devices. Lamberti *et al.* developed a method to create laser scribed graphene on sulfonated poly(ether ether ketone) [152]. The fabricated supercapacitors had specific capacitance of $30mF/cm^2$ and potential window of 3V. El Kady *et al.* used standard DVD burner to reduced graphene oxide [104]. They were able to fabricate more than 100 microsupercapacitors with high power density ($200 W/cm^3$) in less than 30 minutes on a singles disc of graphene oxide. Table 2.2 shows different materials and lasers used in laser scribing as well as its applications.

Table 2.2: Materials and applications for laser scribing

Substrate Material	Conductive Material	Laser	Application	Ref.
Sandpaper	Sandpaper-supported nickel coating (SNC)	Diode laser	Glucose sensor	[153]
PI	B-LSG	CO_2 laser	Microsupercapacitor.	[129]
PI	LSG/MnO_2, LSG/FeOOH, LSG/PANI	CO_2 laser	Pseudo Microsupercapacitor.	[154]

PI	LSG	Diode laser	Sound sensing artificial throat.	[155]
GO	rGO	DVD burner	In-plane transistor, photodetector, speaker.	[156]
PI	LSG/rGO	Diode laser	Strain sensor.	[157]
GO	rGO	Diode laser	Graphene epidermal electronic skin.	[158]
PI	LSG	CO_2 laser	Flexible lithium sulfur battery.	[159]

2.3 Motivation

Interdigitated microsupercapacitors have become the most used designs for commercial wearable MSCs. However, experimental data suggests that the capacitance of these MSC varies with changing dimensions even with no change in surface area of the structure. Various explanations have been given for this change however no conclusive agreement has been reached. By analyzing the effects of electrodes on each other and on the current collector we can more deeply understand the energy storage mechanism in interdigitated MSC and be able to design more optimal structures for higher capacitance.

2.4 Aims and Objectives

1. Fabrication of single electrode interdigitated microsupercapacitor with different geometries on flexible polyimide substrates.
2. Capacitance analysis of each design using cyclic voltammetry and electrochemical impedance spectroscopy.
3. Simulation of each design on COMSOL Multiphysics to study the effect of change in electric field in the structure and its effect on capacitance.
4. The capacitance variation with changing dimensions should be linear for both experimental and simulation data.
5. The capacitance measured for single electrode design must linearly scale up for multi-electrode structure.

CHAPTER 3: METHODOLOGY

3.1 EXPERIMENTATION

We fabricated interdigitated microsupercapacitors using laser scribing technology on flexible polyimide substrate. H_3PO_4/PVA polymer gel electrolyte was used for the experiments.

3.1.1.   MATERIALS

Materials required for fabrication of interdigitated MSC and electrolyte synthesis are mentioned below:

- 0.25mm polyimide sheet (acquired from Chinese supplier).
- Kapton tape (acquired from DuPont).
- Deionized (DI) water.
- H_3PO_4 (acquired from Sigma Aldrich).
- Polyvinyl alcohol (PVA) powder (acquired from Sigma Aldrich).

3.1.2.   INSTRUMENTS

Instruments used for the fabrication, testing, material characterization of interdigitated MSC and electrolytes are mentioned below:

- OSRAM diode laser ($\lambda = 410$nm).
- STOE θ-θ XRD diffractometer.
- JEOL Analytical SEM (JSM-6490A).
- Biologic EC-LAB (VSP).
- FTIR.
- Optical Microscope (Optika Microscopes).
- Optical Profilometer.
- Hot plate stirrer (VELP).

3.1.3.   FABRICATION OF MICROSUPERCAPACITOR

Structures for microsupercapacitor consisted of three designs, each of which had 4 structures with one varying parameter. The structure designs are shown in figures 3.1-3.3. These structures were first drawn on AutoCAD and converted into .bmp files to allow importing on laser software. Next, polyimide sheets, cut in 5x2 cm rectangles, were placed on the stage for diode laser and software with required image was used to pattern the polyimide substrate as shown in figure 3.4 (a). Once the design was traced by the laser it was run again to fill any gaps. Figure 3.4 (b) shows the laser system used.
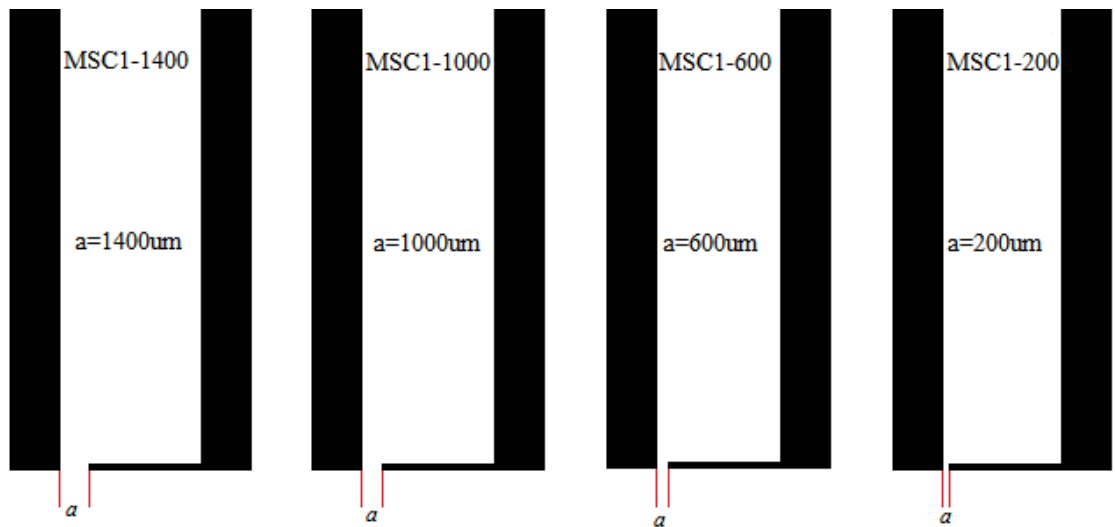
Figure 3.1: MSC1 (with distance between electrode and current collector as the varying parameter).
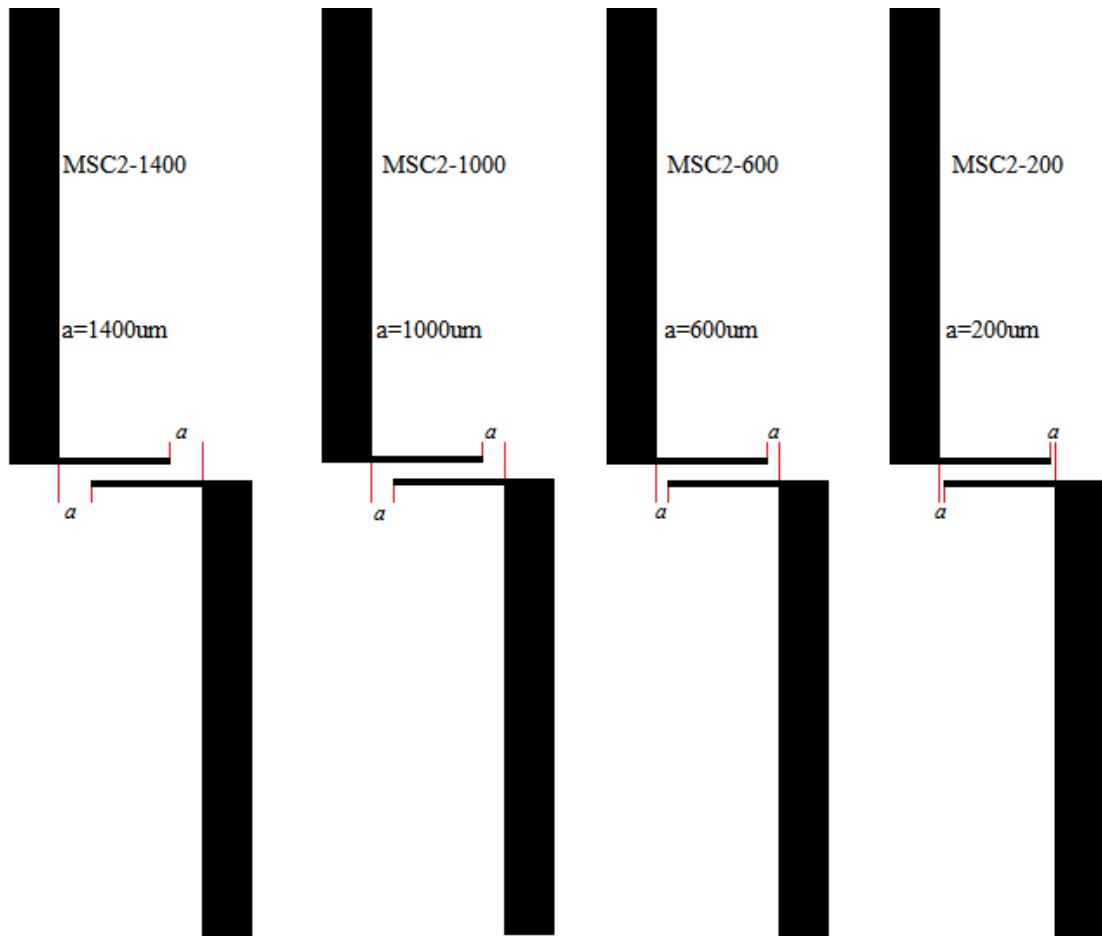
Figure 3.2: MSC2 (with aperture of the supercapacitor as the varying parameter).
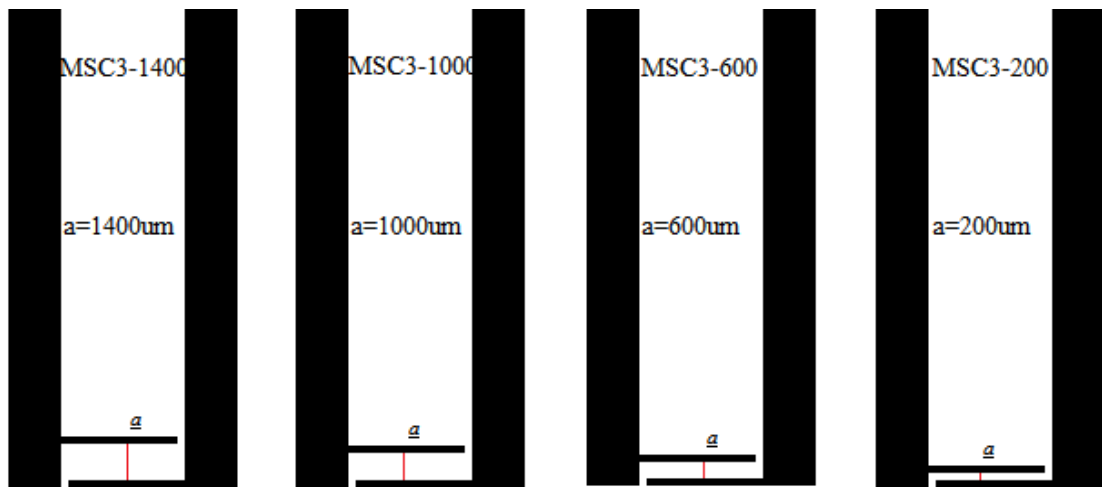
Figure 3.3: MSC3 (with vertical distance between two electrodes as the varying parameter).
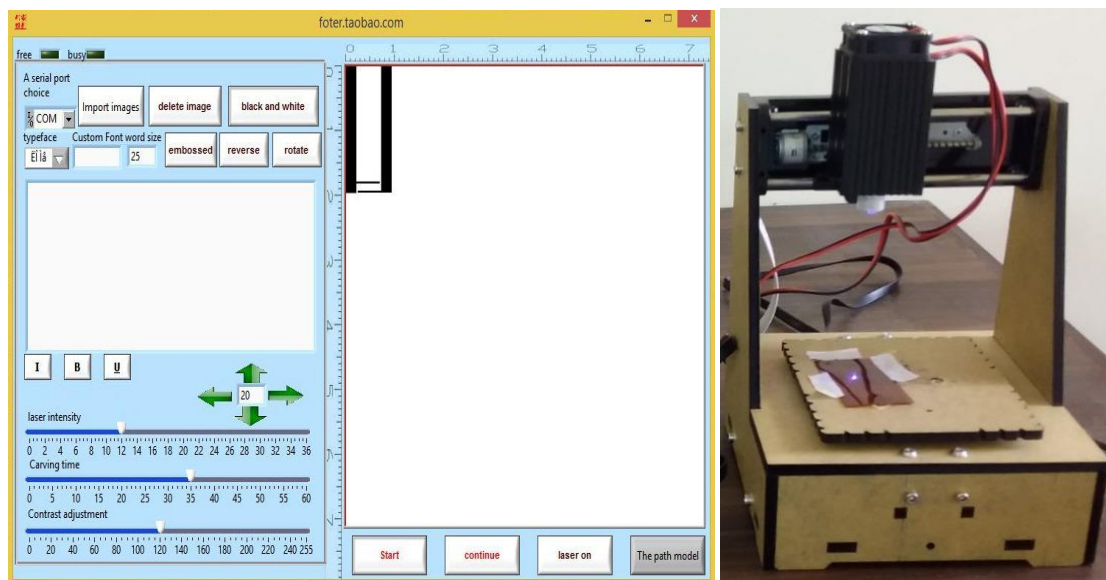
Figure 3.4: (a) Laser scribing software; (b) Laser System in SCME-NUST.

The current collectors were then covered by kapton tape, in order to safeguard them from electrolyte. Electrodes were uniformly coated with electrolyte and covered with kapton tape before testing. The final product is shown in figure 3.5.
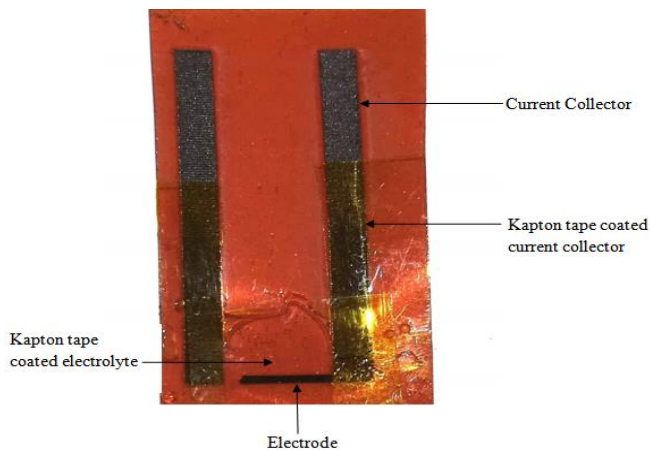
Figure 3.5: Fabricated laser scribed supercapacitor.

3.1.4.   ELECTROLYTE SYNTHESIS

H_3PO_4/PVA gel electrolyte was synthesized by adding PVA (molar mass ~80,000g/mol) powder to deionized water (1g PVA/10g H_2O). The mixture was heated at ~90°C with constant stirring until it turned clear. After cooling to room temperature, 0.8g H_3PO_4

solution was added and the system was stirred and heated to form a viscous homogenous solution.

3.2 SIMULATION

Simulation for each design was done using COMSOL Multiphysics. First, 2D structures were designed using the parameters listed in table 3.1. Note that all the parameters used for simulation were the same as that for fabricated microsupercapacitors.

The material for electrode was chosen to be graphene ($\varepsilon_r = 3$) while H_3PO_4 ($\varepsilon_r = 70$) was chosen as electrolyte. Next, the designed supercapacitors were studied using the AC/DC (electrostatics) physics. Maxwell capacitance was noted for each structure as well as the direction and strength of electric field lines, electric potential contour between current collector and electrode and between two electrodes. The varying parameters for each MSC are described in table 3.2.

Table 3.1: Parameter used for MSC design in COMSOL.

Parameter	Value
Current collector length	20 mm
Current collector width	2.1 mm
Electrode width	0.5 mm
Electrode length	5 mm
Electrolyte width	3*(electrode width)+(gap between electrodes)
Electrolyte length	2*(gap between current collector and electrode)+(electrode length)

Table 3.2: Varying parameter for each MSC.

MSC	Varying Parameter	Values
1	Distance between electrode and current collector.	1400 μm, 1000 μm, 600 μm,200 μm
2	Aperture of supercapacitor.	1400 μm, 1000 μm, 600 μm,200 μm
3	Distance between two parallel electrodes.	1400 μm, 1000 μm, 600 μm,200 μm

CHAPTER 4: CHARACTERIZATION TECHNIQUES

4.1 SCANNING ELECTRON MICROSCOPE (SEM)

In SEM very fine electron beam is focused on a sample surface. The electron-matter interaction causes ejection of photons or electrons from the surface. The ejected electrons enter a detector which modulates the brightness of cathode ray tube (CRT). Every point on the sample is surface is scanned by the electron beam and plotted on the corresponding position in CRT resulting in the image of the surface to be formed. The schematic of a typical SEM is shown in figure 4.1 (a).

SEM uses secondary electrons (SE) to produce image of the surface. These are the electrons which are ejected from the surface atoms upon receiving excitation from the electron beam. The image produced from SE can show details as small as 1 nm. Interaction of electrons with the surface also causes release of backscattered electrons (BSE) and X-rays. BSE are the primary electrons which are ejected as a result of elastic scattering from heavy atom nuclei within the material. However, since BSE come from deeper within the material compared to SE, they are not suitable for surface imaging and can cause decrease in surface resolution. Characteristic X-rays emitted from atoms of materials are used in several techniques to identify material composition.

We have used JEOL-JSM-6490LA see the surface morphology and uniformity of LSG. The details of the system are shown in table 4.1. Figure 4.1 (b) shows the JSM 6490LA SEM used in this work.
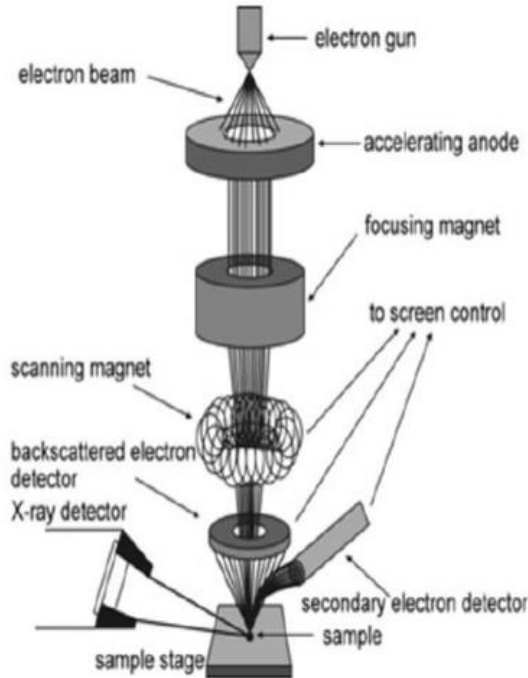
Figure 4.1: (a) Schematic of SEM; (b) JSM 6490LA SEM available at SCME, NUST.

Table 4.1: JEOL-JSM-6490LA system features.

Spot size	35-60
Operating voltage	10-20 KV
Electron source size	10-20 μm
Filament life	50-500 hours
Power	30 kVA
Accelerating voltage	0.3 – 30kV
Working distance	10mm
Highest resolution	3 nm

4.2 X-RAY DIFFRACTION (XRD)

XRD is a versatile technique which uses x-rays incident on a sample to determine the structure of unit cell and find the phases present in it find. X-rays are diffracted by the sample at specific angles determined by lattice planes. Only those x-rays which undergo constructive interference (following Bragg's law) after diffraction are detected. The

intensity of the x-ray diffraction peak is determined by atom distribution inside the lattice and thus it can be used to determine the crystalline structure of the material. Bragg's law states that:

$$n\lambda = 2dSin\theta$$

When, λ is X-ray wavelength (determined by anode material), d is the inter plane distance, n is a positive number and θ is diffraction angle. Figure 4.2 (a) shows schematic for x-ray diffraction.

X-rays are produced by striking an anode with very high energy electrons anode in a vacuum chamber. The electrons are produced by electrically heating a filament. Anodes are usually made of Mo, Cu or Fe. XRD analysis done in this work was performed by STOE diffractometer in 2θ range of 5-40 degrees at SCME-NUST (figure 4.2 (b)).
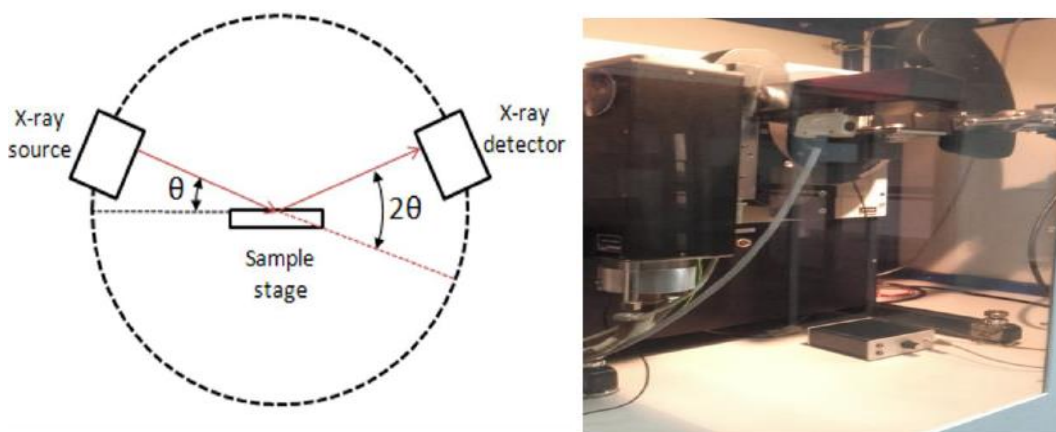
Figure 4.2: (a) Working of XRD; (b) XRD diffractometer at SCME-NUST.

4.3 FOURIER TRANSFORM INFRARED SPECTROSCOPY (FTIR)

This technique is used for analysis of organic materials, polymers, food products etc. Infrared light incident on the sample is absorbed by it and cause vibration of molecule energy levels. The amount of energy absorbed is determined by the gap between energy levels. The remaining light is reflected back and an absorption spectrum is generated to determine the molecular structure. FTIR can be readily used for solid, liquid and gas

analysis with little to no sample preparation required. The absorption spectra usually lie in the 4000-400 cm^{-1} for most organic and inorganic materials.

FTIR spectrometer has a light source (in infrared region), an interferometer and sample holder with detector. In addition amplifier, analog-to-digital convertor and computer are used for image processing, Fourier transformation and to view the absorption spectrum. Light from the source is split into two components the first of which is reflected back while the second beam passes through the interferometer to the sample and is collected by the detector. The difference in intensity of the two light beams determines the amount of energy absorbed and absorption spectrum is generated by the computer after Fourier transformation. Figure 4.3 shows the working of a FTIR and the system used for this work.
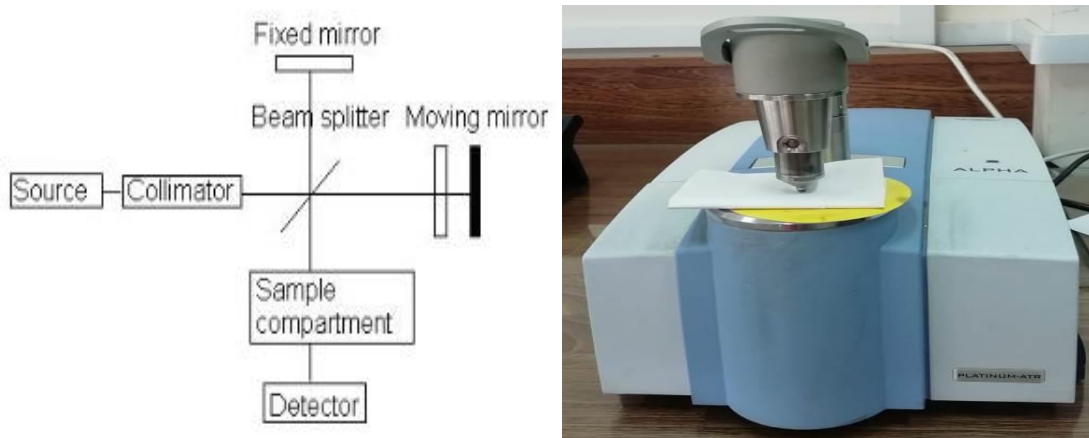
Figure 4.3: (a) Working of FTIR; (b) FTIR spectrometer in SNS NUST.

4.4 OPTICAL PROFILOMETER

Optical profilometry is used to determine the height and surface roughness of a sample without damaging it. The profilometer consists of an optical light source, beam splitter, sample holder, mirrors and detector/camera. Light of known wavelength from the source is split into two beams. The first beam is reflected from a reference mirror while the second is bounced back from the test sample. The two beams are then recombined and undergo constructive or destructive interference to cause light or dark interference

fringes. Since the roughness of the reference mirror is known (as smooth as possible), the difference in optical paths of the two reflected beams is due to the height of the test sample. With the knowledge of light wavelength the height variations on the surface of test sample can be determined and used to construct a 3D map of the surface. Figure 4.4 shows the working of an optical profilometer.
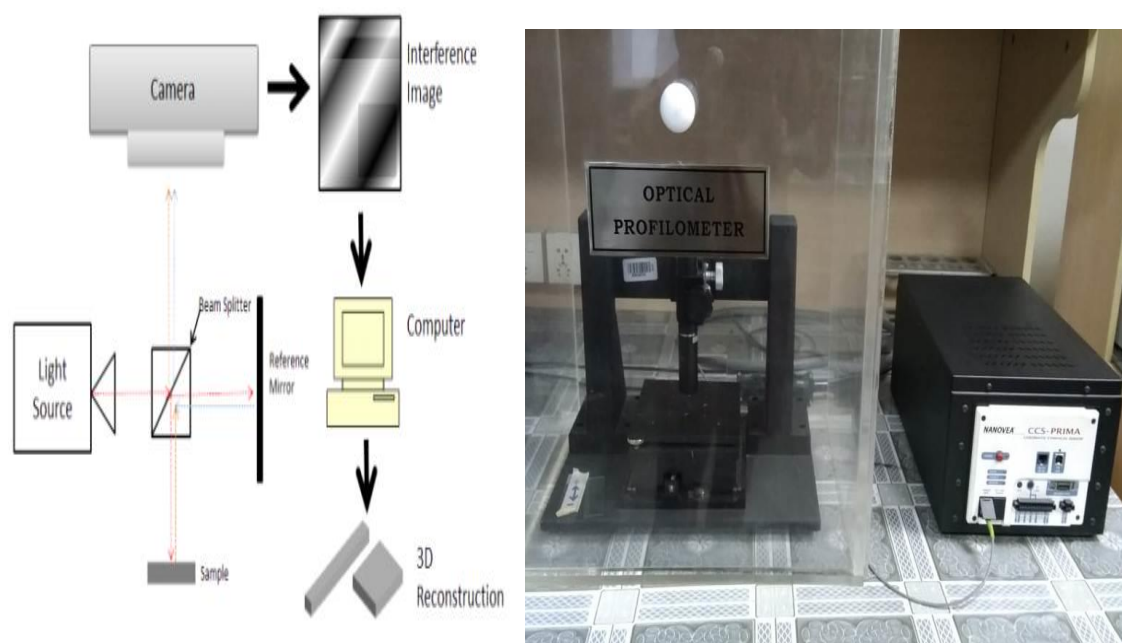
Figure 4.4: (a) Working of Optical Profilometer; (b) Optical Profilometer at SCME-NUST.

4.5 CYCLIC VOLTAMMETRY (CV)

This is the most commonly used method to study the electrochemical behavior of a material or system. Voltage is ramped up to a E_2 and back again to initial voltage E_1 and the response current is measured. The magnitude of the current depends on the type of process taking place at the electrode and on the concentration as well as current carrying capability of analyte in the electrolyte solution. The rate at which voltage is changed is called scan rate of the experiment and is measure in V/s. For higher scan rates the IV curve shows distortion of CV curve (called cyclic voltammogram) from its ideal shape due to incomplete redox reactions or incomplete double layer formation. Figure 4.5 shows the applied voltage and resulting current in a cyclic voltammetry experiment.

The CV system has a potentiostat connected to three electrodes called working electrode (WE), reference electrode (RE) and counter/auxiliary electrode (CE). Potential is applied between WE and RE while response current is measured between WE and CE. For two electrode system the counter and reference electrodes are the same. The voltammogram are plotted directly by simulation software (such as EC-Lab). When linear sweep voltage is applied to an ideal supercapacitor the generated current (I) is dependent on the rate of voltage sweep ($\frac{dV}{dt}$) and on the capacitance of the system (C).

$$I = \frac{dQ}{dt} = C\,\frac{dV}{dt}$$
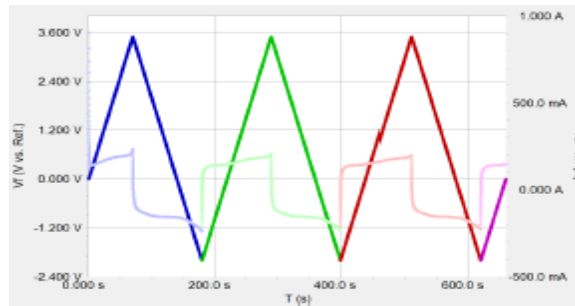
Figure 4.5: Voltage and current values versus time for cyclic voltammetry.

4.6 ELECTROCHEMICAL IMPEDANCE SPECTROSCOPY (EIS)

This technique is primarily used to determine ESR value of a supercapacitor. A small AC excitation signal is supplied to electrochemical cell and response current is measured. Ideally the current should have the same frequency as the input signal with phase shift. The input and output signals are then used to find the impedance of system by using Ohm's law:

$$Z = \frac{V}{I} = \frac{Vo\ Sin(\omega t)}{Io\ Sin\ (\omega t + \phi)} = Zo\,\frac{Sin(\omega t)}{Sin\ (\omega t + \phi)}$$

Impedance of the system can be plotted in several ways. If the real and imaginary parts of impedance are plotted on X and Y axis respectively then a semi circle is formed on which overall impedance is the length of vector Z as shown in figure 4.7 (a). This is

called a Nyquist plot. On the other hand if the log of impedance (log Z) is plotted against frequency then it is called a Bode plot (figure 4.7 (b)). Figure 4.8 shows combined CV and EIS system in SCME-NUST.
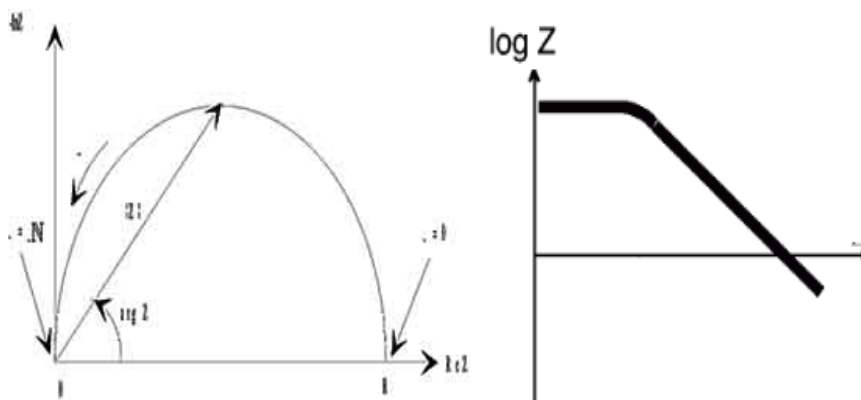
Figure 4.6: (a) Nyquist plot (b) Bode plot

Figure 4.7: Combined CV and EIS system in SCME-NUST.

CHAPTER 5: RESULTS AND DISCUSSION

5.1.   MATERIAL CHARACTERIZATION

The fabricated microsupercapacitors and electrolytes were tested to determine formation of required material. MSCs were tested using XRD, SEM, optical microscope as well as optical profilometer in order to determine the structural phases of the laser scribed graphene, surface morphology of LSG, dimensions of the fabricated MSCs and height of the LSG film respectively. The synthesized electrolytes were characterized using FTIR.

5.1.1. SCANNING ELECTRON MICROSCOPE

Figure 5.1 shows the structural characterization of the fabricated LSG at different magnifications (100x, 500x, 2500x and 10,000x). At higher resolutions shown in figure 5.1 (c) and (d) the overlapped layers of graphene are clearly visible. This overlapping of layers is responsible for the increased conductivity of LSG.

Figure 5.2 shows the cross sectional view of the same sample. It is observed that LSG is formed only on the surface of PI. Thickness of LSG on PI depends on laser power. For this work the optimal laser power was 106mW.
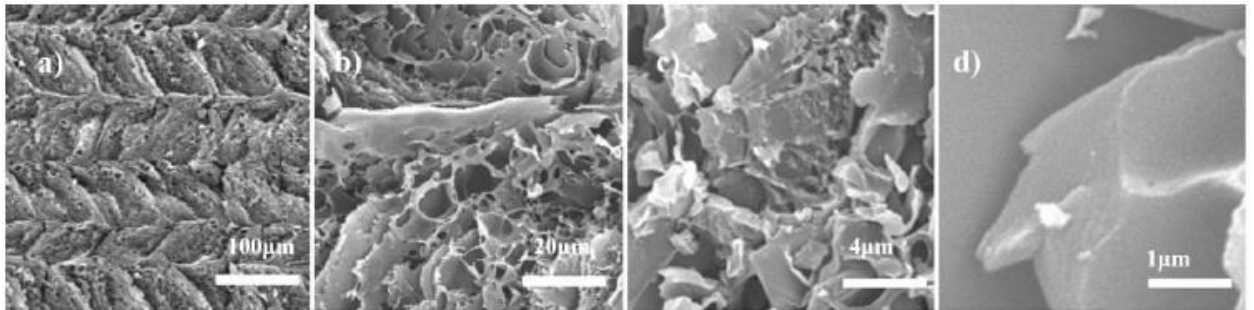
Figure 5.1: SEM images for LSG at various magnifications.
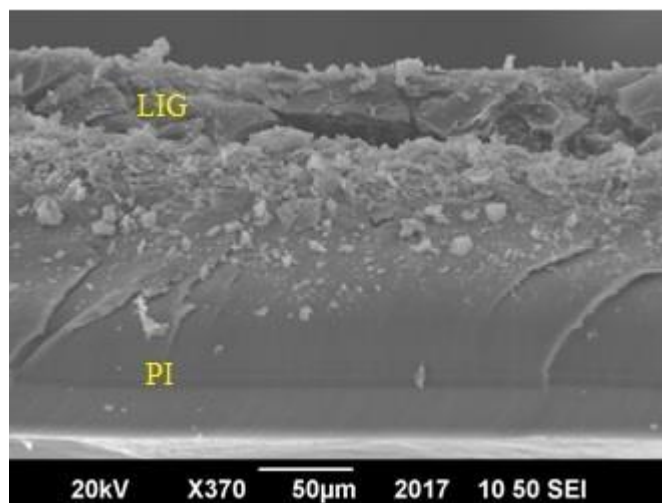
Figure 5.2: Cross sectional view of LSG on PI.

5.1.2.   X-RAY DIFFRACTION

XRD analysis was performed before and after laser scribing of polyimide sheet as shown in figure 5.3. LSG XRD data shows some crystalline peaks along with broader region making the structure semi-crystalline. Figure 5.3 (b) shows the XRD of the LIG powder scraped off of polyimide. The peak at 24.9° shows that the structure formed is carbonaceous structure. The broadening of the peaks shows that the structure is graphene like as it is not a sharp peak.
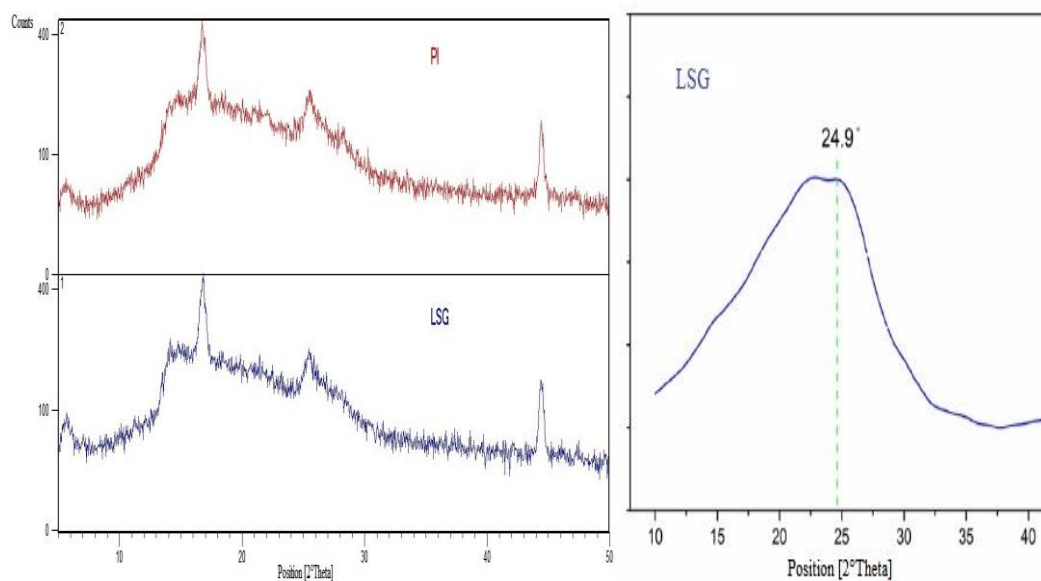
Figure 5.3: (a) XRD analysis before and after laser scribing; (b) XRD of LSG powder scrapped off PI.

5.1.3. FOURIER TRANSFORM INFRARED SPECTROSCOPY

FTIR analysis was done after the synthesis of H_3PO_4/PVA electrolyte. Results are shown in figure 5.4. Broad peak near 3300 cm^{-1} and the small dips near 2900 and 2300 cm^{-1} show the presence of PVA. Absorbance peaks at 2800-3000 and 2400 cm^{-1} as well as the sharp vibrational peaks near 1700, 1450 and 1000 cm^{-1} are indicative of presence of H_3PO_4.
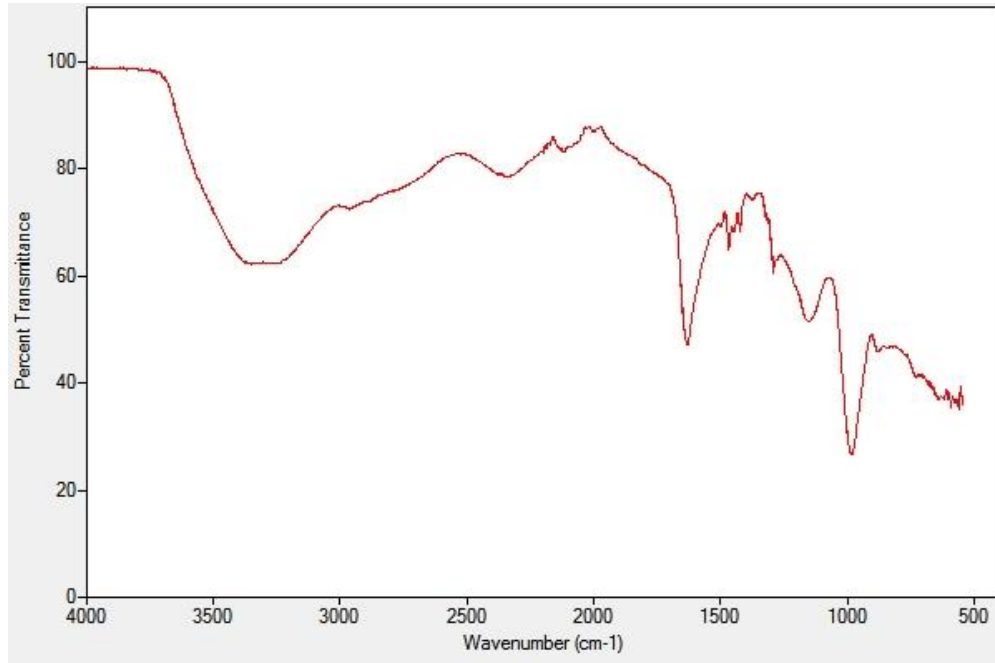
Figure 5.4: FTIR Spectrum of H_3PO_4/PVA electrolyte.

5.1.4. OPTICAL PROFILOMETRY

Optical profilometer was used to determine the height of the LSG. Two samples were characterized using this technique. Sample 1 was MSC fabricated by tracing laser over polyimide sheet only once using 106mW laser power. This MSC had significantly less conductivity than the MSC fabricated by tracing the laser over PI twice. The thickness of LSG was 31.9 μm which resulted in significantly less surface area and hence decreased capacitance for the MSC.

Sample 2 had laser traced twice over the PI sheet at 106mW power and provided the best conductivity. Thickness of LSG for this sample was 46.798μm which was 68.15% more than sample 1. This also meant an increase in active surface area of the MSC

which directly corresponds to increased capacitance. Optical profilometry results of the two samples are shown in figure 5.5.

Maximum height	72315 nm
Mean height	31904 nm
Width	1.01 mm

Maximum height	70637 nm
Mean height	46798 nm
Width	1.03 mm
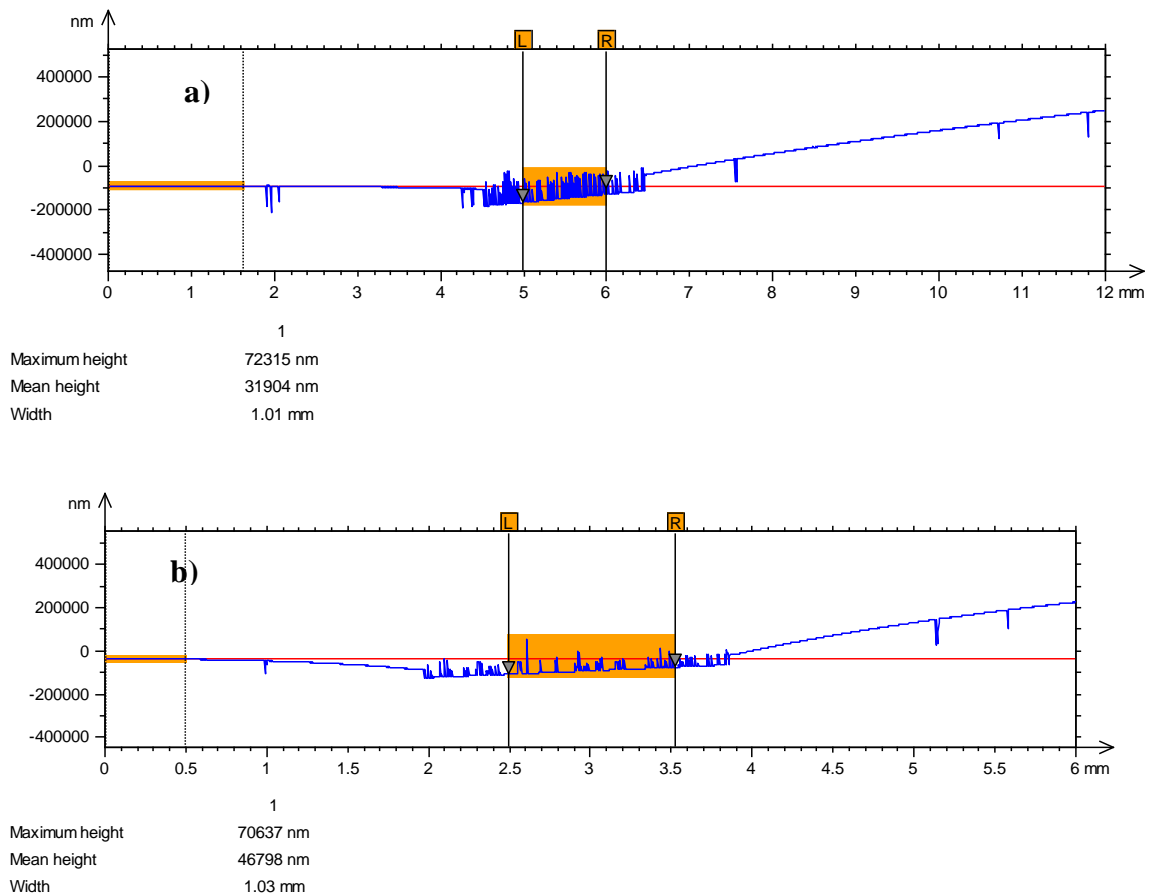
Figure 5.5: Optical profilometer profile for (a) sample 1 and (b) sample 2.

5.2.   LASER CHARACTERIZATION

Laser characterization was done at National Centre for Physics and Quaid-e-Azam University, Islamabad. The laser system and software used in this work is shown in figure 5.6. It has 410nm wavelength (with 1.5nm width) and maximum power of 127mW as shown in figure 5.7. For this work the laser was used at 106mW power.
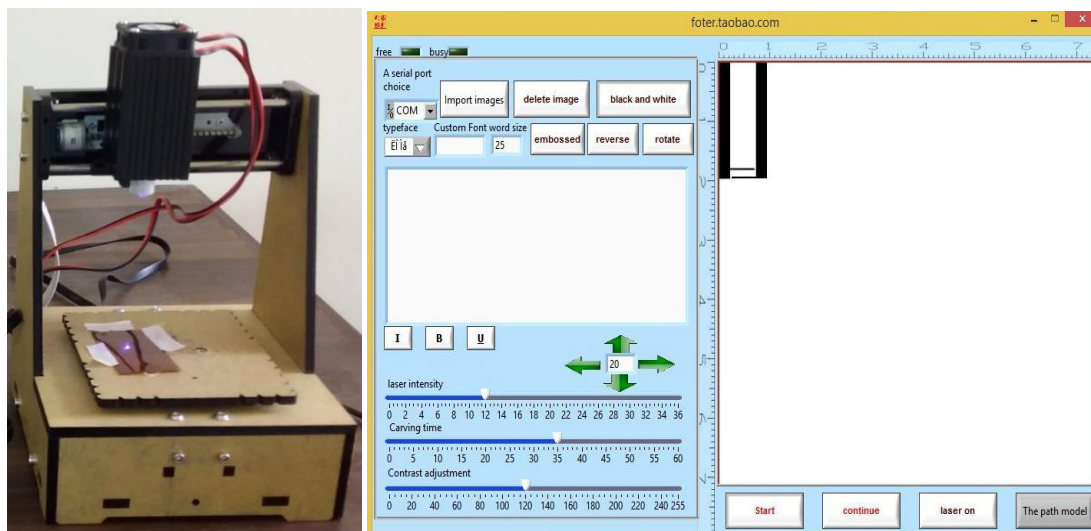
Figure 5.6: (a) Laser system and; (b) Software used in this work.
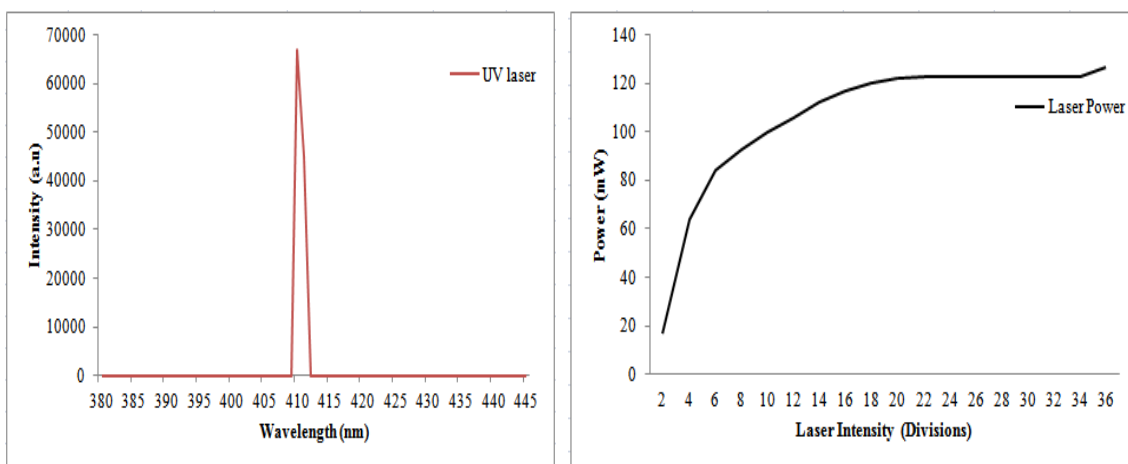
Figure 5.7: (a) Wavelength vs. Intensity plot; (b) Intensity vs. Power.

Vast amount of research work has been done in order to identify the mechanism of laser reduction [160-163]. It was found that the process involved in surface reduction depends upon the wavelength of laser used. For lasers with wavelength >390nm, photothermal reduction is the chief mechanism involved in surface reduction. This means that laser irradiation can cause high temperature, in the range of ~2500-3000°C, at the surface which provides enough energy to break C-O, C=O and C-N bonds and leads to the formation of conductive C-C bonds at the surface. If the wavelength of laser is <390nm photochemical reduction is the dominant mechanism. However, this mechanism is always accompanied by photothermal effect. When high energy laser is irradiated on the surface of a polymer (>3.2eV; λ<390nm) electronic excitation takes place which causes

breaking of C-O, C=O and C-N bonds and eventual removal of oxygen and nitrogen from the surface. When excited electrons relax, and recombination takes place, a large amount of heat is released which leads to further reduction caused by photothermal effect. For this work the mechanism involved in reduction of polyimide is clearly photothermal effect.

5.3.   DEVICE CHARACTERIZATION
5.3.1. MSC1

MSC1 was designed in order to study the relationship between electrode and current collector. Since the LSG serves as both electrode and current collector material, the latter was insulated using Kapton tape in order to prevent double layer formation on its surface. We expected electric field to be induced between the oppositely charged electrode and current collector during charging which would result in small electrostatic capacitance to be induced between the two, in addition to the double layer capacitance at the electrode. In order to test this hypothesis we steadily decreased the distance between electrode and current collector without changing size of electrode or any other parameter that would result in decreased surface area for EDLC formation at the electrode. As the distance between the current collector and electrode decreased we observed a noticeable increase in overall capacitance. Since the tests were performed using only one electrode for the MSC it eliminated the possibility of change in capacitance due to change in diffusion path between two electrodes. Thus the change in capacitance must be due to the increased electrostatic capacitance between current collector and electrode as the distance between the two decreases. Figure 5.8 shows the optical micrograph for MSC1.
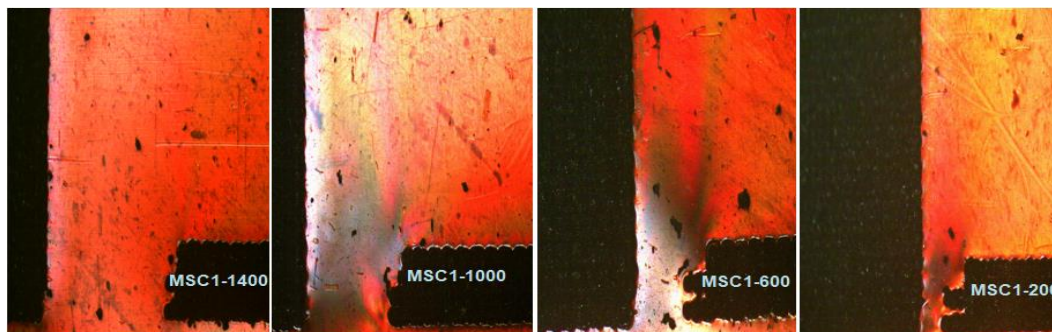
Figure 5.8: Optical Micrographs of MSC1.

5.3.1.1. Cyclic Voltammetry

Figure 5.9 shows the cyclic voltammogram for MSC1 and figure 5.10 shows the trend of increase in capacitance as the distance between electrode and current collector decreases. The total capacitance is calculated using the formula:

$$C = \frac{\int I \, dV}{k \, \Delta V \, A} \quad\quad\quad (1)$$

Where,

C is the total capacitance of the system,

$\int I \, dV$ is the discharge current,

k is the scan rate,

ΔV is the voltage range of the measurement, and

A is the total area of the capacitor.

Figure 5.10 shows that as the distance between electrode and current collector decreases from 1000μm to 600μm there is a sharp increase in total capacitance of the system. This has been found to be due to decrease in R_{AB} as defined in section 5.3.1.2.
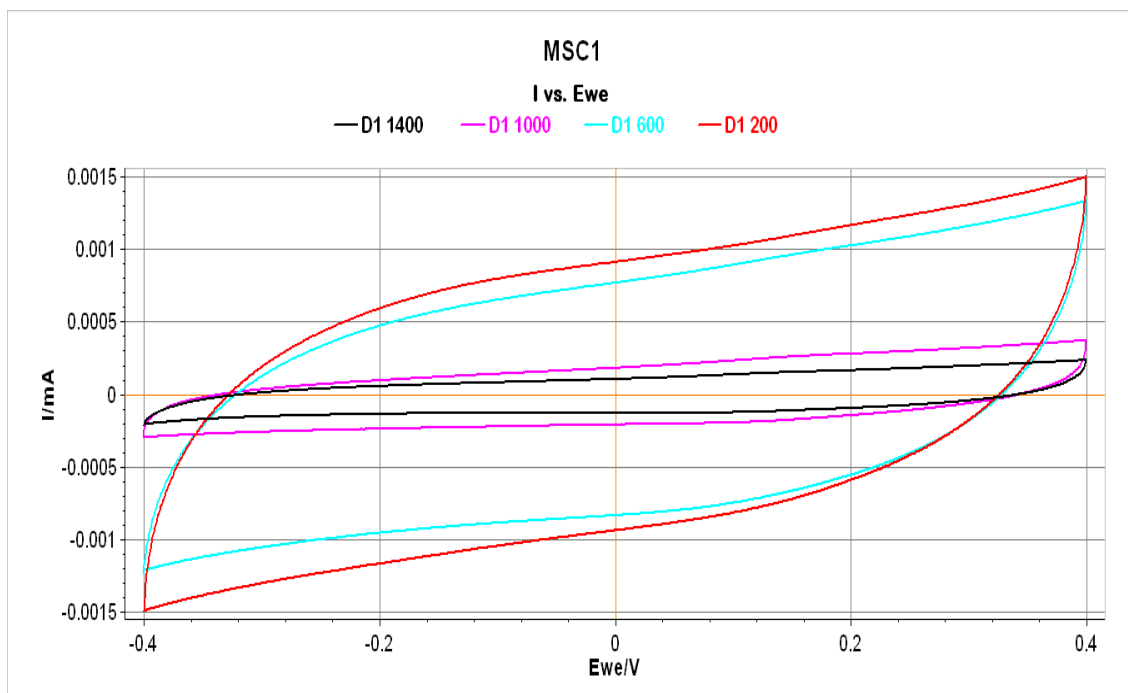
Figure 5.9: Cyclic Voltammogram for MSC1.
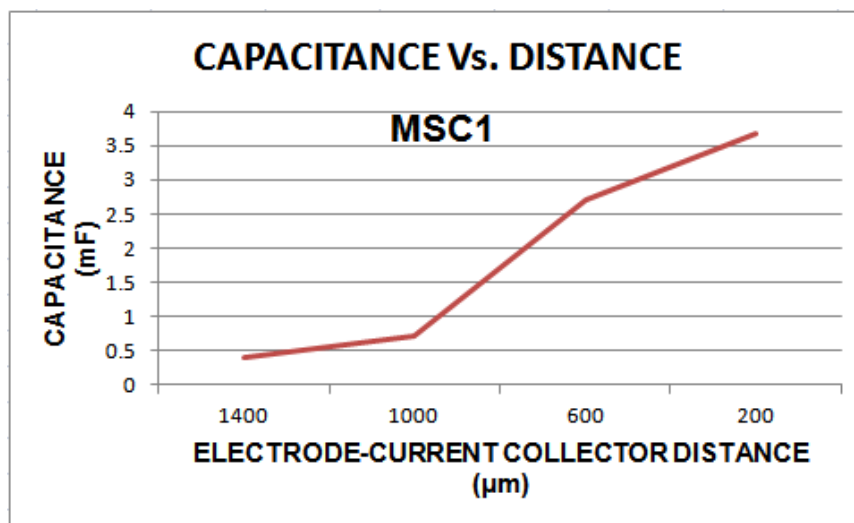
Figure 5.10: Capacitance vs. Electrode-Current Collector Distance for MSC1 (Calculated from Cyclic Voltammetry).

5.3.1.2. *Electrochemical Impedance Spectroscopy*

EIS measurements were done to extract more information about the working of MSC. Typical Nyquist plot for EDLC is shown in figure 5.11. Resistance R_A is defined in literature as one of or sum of ohmic resistance of electrolyte in the pores of porous electrode, electrode material resistance and resistance due to the material mismatch at electrode-current collector interface [138, 164]. Any one of these resistances or the sum of these three is often called Equivalent Series Resistance (ESR) of the supercapacitor. In this work the electrode and current collector are both made of LSG hence there is no effect of mismatch contact resistance and R_A is defined as the sum of electrolyte resistance in pores of electrode and electrode resistance. R_{AB} is often referred to as charge transfer resistance attributed to length of ion diffusion pathway between two electrodes [138, 165-168] or as polarization resistance which is defined as resistance encountered by the electrolyte ions during penetration inside the electrode [164, 169, 170]. R_B is the sum of resistances R_A and R_{AB}. R_C is defined as the overall resistance of the device [171, 172]. The line BC typically has an angle of 45° with the real axis and shows the variation of EDLC from ideal capacitive behavior [104, 168]. At low frequency an ideal EDLC has dominant capacitive behavior as shown by straight line beyond C in figure 5.11 [171-175].
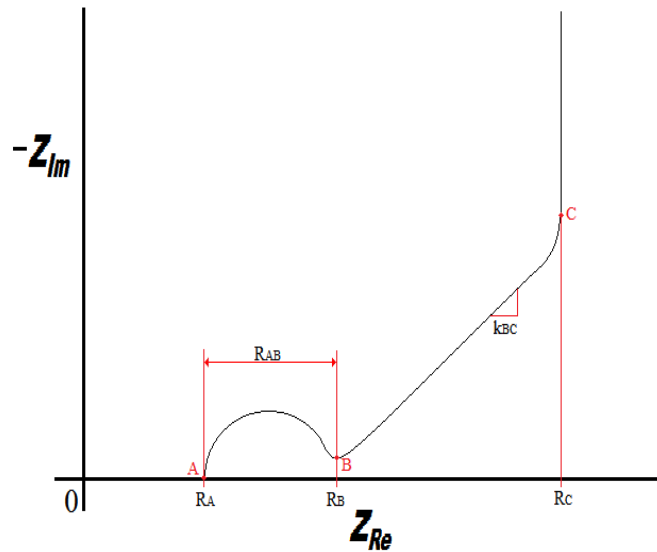
Figure 5.11: Typical Nyquist plot for EDLC.

Figure 5.12 shows EIS results for MSC1 and the values obtained from EIS analysis are shown in Table 5.1. The value of R_A decreases as distance between current collector and electrode is decreased. This shows that R_A is effected by an additional parameter in addition to the three defined above. This might be due to electric field being produced between the current collector and edge of electrode which induces an electrostatic capacitance between the two. As the distance between the electrode and current collector increases the electric field strength decreases causing increase in R_A and as the distance increase from 200µm to 600µm R_A drops more than 2kΩ after which it experiences somewhat saturation possibly due to sharp decrease in electric field. Since electric field is experienced only at the edge of the electrode, its effect on electrolyte and electrode surface resistance is not very pronounced and thus it is not the dominant factor for decrease in capacitance for MSC1. Also, the decrease in R_A is not as pronounced as that in MSC2 and MSC3 for the same reason. Note that the surface area of device, electrolyte concentration and laser parameters were kept constant for all MSCs so as not to cause change in capacitance due to double layer effect.

R_{AB} also increases as the distance between electrode and current collector increases. we suggest that electric field between the edge of electrode and current collector causes the surface resistance of electrode to decrease [176, 177] thus decreasing the polarization resistance by providing a less resistive path to ion transport inside the pores of the electrode. As the distance between current collector and electrode decreases the electric field increases leading to decrease in electrode surface resistance and consequently decrease in polarization resistance. At distance greater than 600µm there is a significant increase in R_{AB} which might be due to sharp decrease in electric field at this distance which in turn causes decrease in capacitance as evident from cyclic voltammetry curves.

The next parameter analyzed is the slope of line BC (k_{BC}). k_{BC} is defined as the ratio between time constants τ_D and τ_{RC}, ($k_{BC} = \tau_D / \tau_{RC}$) [178], where

$$\tau_D = \frac{L^2}{D}$$

$$\tau_{RC} = (R_{EB} + R_D)C_{diff}$$

τ_{RC} corresponds to the behavior of an ideal RC circuit with resistance ($R_{EB}+R_D$) in series with a capacitor with total differential capacitance C_{diff}. In the case of EDLC R_{EB} and R_D are defined as bulk electrolyte resistance and diffuse layer resistance respectively. τ_D is the time constant corresponding to the diffusion of electrolyte ions and depends on the total length covered by the electrolyte (L) and the diffusion coefficient (D) of the electrolyte [178]. It has been proven that as the electric field increases the diffusion coefficient of the electrolyte decreases due to highly resistive path experienced by the electrolyte ions in the region of electric field [179]. When the electrode is very close to the current collector (distance ~200μm) the electric field experience by it is very large compared to when it further from the current collector. This high electric field causes a decrease in the diffusion coefficient which in turn increases τ_D and consequently causes high k_{BC}. As the distance between the current collector and electrode decreases, D increases and results in decreased value of τ_D and k_{BC} as shown in table 5.1. It needs to be mentioned here that though the electric field strength decreases drastically at distances larger than 600μm, it is still present and is large enough to effect D.

It should be noted that the EIS results from this work do not show straight line at lower frequencies corresponding to behavior of ideal RC circuit due to highly porous nature of the LSG electrode.

Figure 5.12: Nyquist plot for MSC1.

Table 5.1: Values of parameters extracted from Nyquist plot of MSC1.

	R_A (kΩ)	R_{AB} (kΩ)	k_{BC}
MSC1-1400	19.51	9.306	0.502
MSC1-1000	18.77	8.446	0.7824
MSC1-600	18.6	5.055	0.9303
MSC1-200	16.74	4.759	1.126

5.3.1.3. Simulation

Figure 5.13 shows the simulation result for MSC1. The electrostatic capacitance obtained for each structure is noted in table 5.2 with figure 5.14 showing the trend of increasing capacitance as the distance between the electrode and current collector decreases due to increase in electric field between the two. Note that simulation was done solely to examine the electric field strength between current collector and electrode

and does not include electric double layer capacitance. As can be seen from figure 5.14 there is an exponential increase in electrostatic capacitance at electrode-current collector distances smaller than $600\mu m$ due to high electric field. As mentioned in section 5.3.1.1 and 5.3.1.2 there is also a sharp decrease in R_{AB} and sudden increase in total capacitance. Thus it can be concluded that at distances smaller than $600\mu m$ the electric field strength is very high which causes electrostatic capacitance between current collector and electrode and also effects certain parameters responsible for double layer capacitance such as electrode resistance and diffusion coefficient causing an increase in it.

Figure 5.13: Simulation results for MSC1.

Table 5.2: Electrostatic Capacitance calculated from Simulation of MSC1.

	Capacitance (nF)
MSC1-1400	0.70058
MSC1-1000	0.91425
MSC1-600	1.3378
MSC1-200	2.8582

DISTANCE Vs. CAPACITANCE
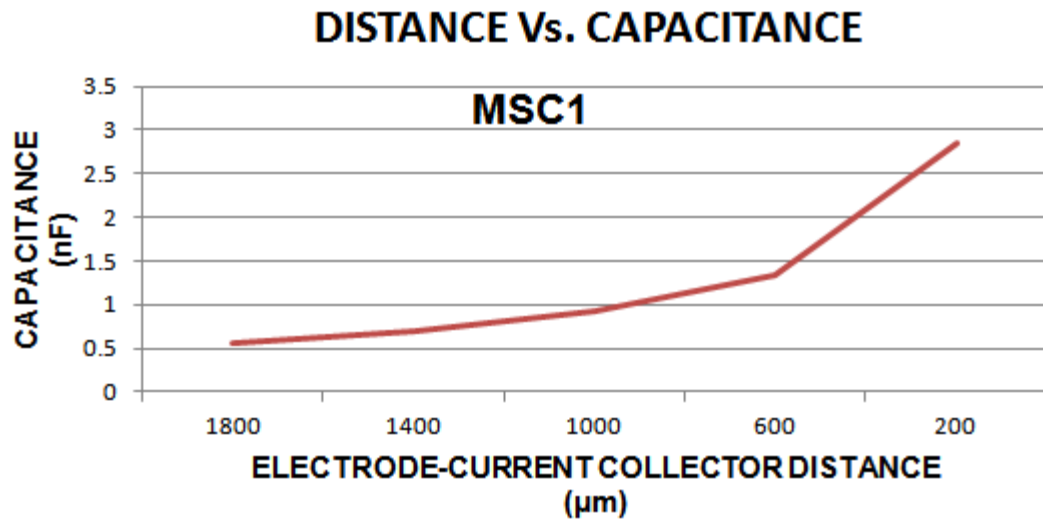
Figure 5.14: Capacitance vs. Electrode-Current Collector Distance for MSC1 (Calculated by COMSOL Simulation).

5.3.2. MSC2

MSC2 was designed to study the relationship between two overlapping electrodes and how the area of overlapping (also called aperture) affects the capacitance of EDLC. Optical micrographs for MSC2 are shown in figure 5.15. Similar to the structures made for MSC1, the current collector was covered with Kapton tape in order to present double layer formation on its surface.

Figure 5.15: Optical Micrographs of MSC2.

5.3.2.1.   Cyclic Voltammetry

Figure 5.16 and 5.17 show the cyclic voltammogram and trend of increase in capacitance for MSC2 respectively. The capacitance is calculated using equation (1). It is evident from the graphs that there is a linear increase in capacitance as the aperture of the two electrodes increases. This has been found to be due to increase in electric field inside the MSC which increases linearly as more and more area of the two electrodes overlaps. The cause of the increase in capacitance is explained in depth using EIS analysis in section 5.3.2.2 and simulations in section 5.3.2.3.
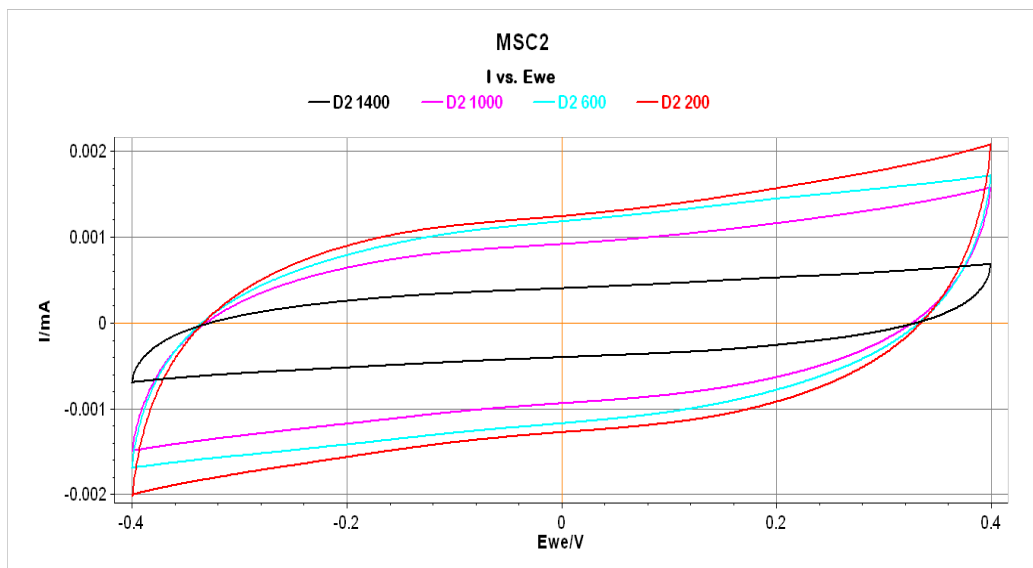
Figure 5.16: Cyclic Voltammogram for MSC2.
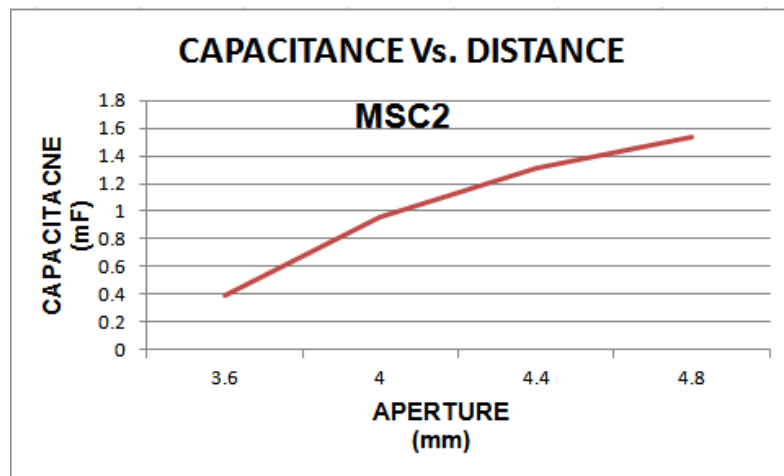
Figure 5.17: Capacitance vs. Aperture for MSC2 (Calculated from Cyclic Voltammetry).

58

EIS graph for MSC2 is shown in figure 5.18 and the extracted information is shown in table 5.3. Similar to the data obtained for MSC1, we observed a decrease in R_A and R_{AB} as the aperture increase while simultaneously there is an increase in the slope of line BC (k_{BC}). The aperture of the two electrodes increases from approximately 3.6mm to 4.8mm from MSC2-1400 to MSC2-200 respectively. The percent change in overlapping area was found to be 33.33% while the change in R_A and R_{AB} was 45% and 66.2% from MSC2-1400 to MSC2-200 respectively. This implies that in addition to longer ion diffusion path for MSC2-1400 there is another force causing decrease in R_A and R_{AB}. From simulation we have seen that there is electrostatic field present between the two electrodes and as the aperture increases so does the electrostatic field. Simulation results found that the increase in electrostatic capacitance from MSC2-1400 to MSC2-200 was 17.6%. Accounting for ±5% variation in experimental and simulation results, it can be estimated that electrostatic field between the two electrodes might cause change in R_A and R_{AB} under the same effects as mentioned in section 5.3.1.2. However, for MSC2 there is also change in ion diffusion pathway between electrodes which plays a role in decreased R_A and R_{AB} while this effect is not present in MSC1.

There is also a drastic increase in k_{BC} from MSC2-200 to MSC2-1400 which can be explained by the same reasoning as that in section 5.3.1.2. However, the change in k_{BC} from MSC2-200 to MSC2-1400 is ~10% larger than that for MSC1. This can be due to electrostatic field being present in larger area for MSC2 compared to the small area of electrostatic field between edge of electrode and current collector for MSC1.
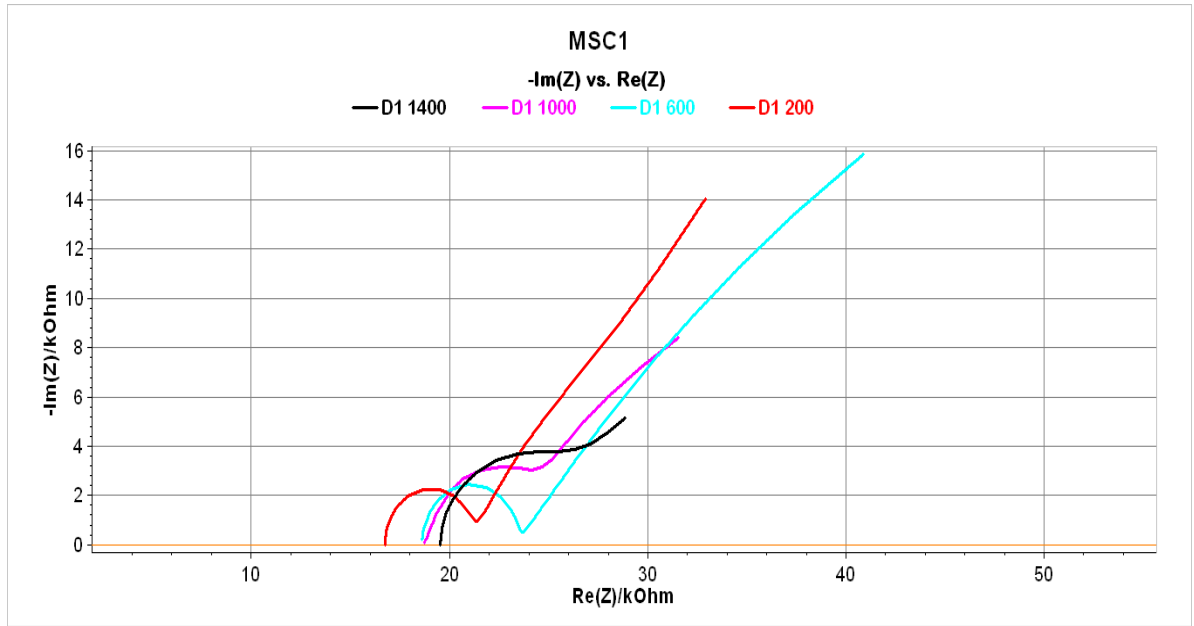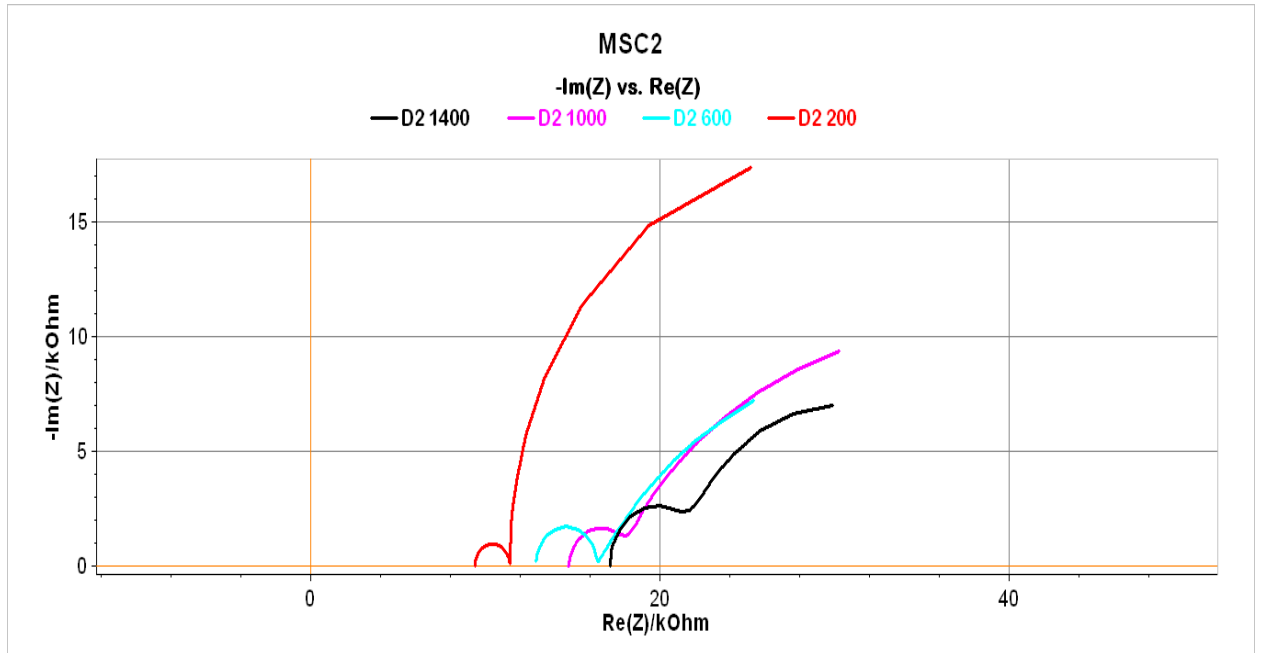
Figure 5.18: Nyquist plot for MSC2.

Table 5.3: Values of parameters extracted from Nyquist plot of MSC2.

	R_A (kΩ)	R_{AB} (kΩ)	k_{BC}
MSC2-1400	17.12	5.891	0.5864
MSC2-1000	14.75	4.041	0.7
MSC2-600	12.88	3.551	0.8432
MSC2-200	9.419	1.987	1.374

5.3.2.3.   Simulation

Figure 5.19 shows the simulation results for MSC2. Similar to EIS and CV results there is a linear increase in electrostatic capacitance as the aperture increases (figure 5.20). We suggest that this linear increase in electric field between the two electrodes causes a linear increase in R_A and C as evident from EIS and CV graphs for MSC2. In this case there is no sharp decrease in electric field between the electrodes because the distance between them remains constant and as the total area which experiences electric field increases so does the electrostatic capacitance as shown below.
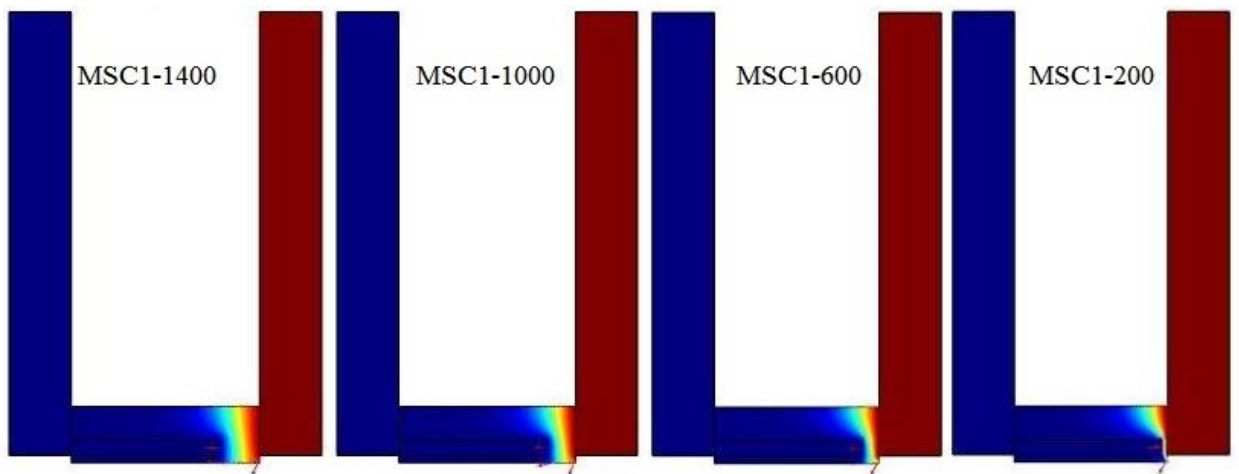
Figure 5.19: Simulation result for MSC2.

Table 5.4: Electrostatic Capacitance Calculated from Simulation of MSC2.

	Capacitance (nF)
MSC2-1400	7.4829
MSC2-1000	8.0269
MSC2-600	8.4931
MSC2-200	8.8026
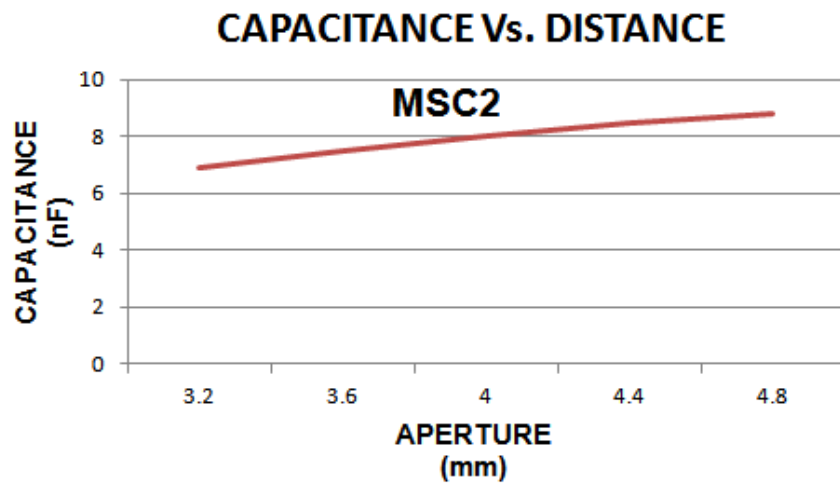
Figure 5.20: Capacitance vs. Aperture for MSC2 (Calculated by COMSOL Simulation).

5.3.3. MSC3

MSC3 was designed to study the effects of interelectrode distance on the total capacitance of the device. Figure 5.21 shows the optical micrographs for this MSC.
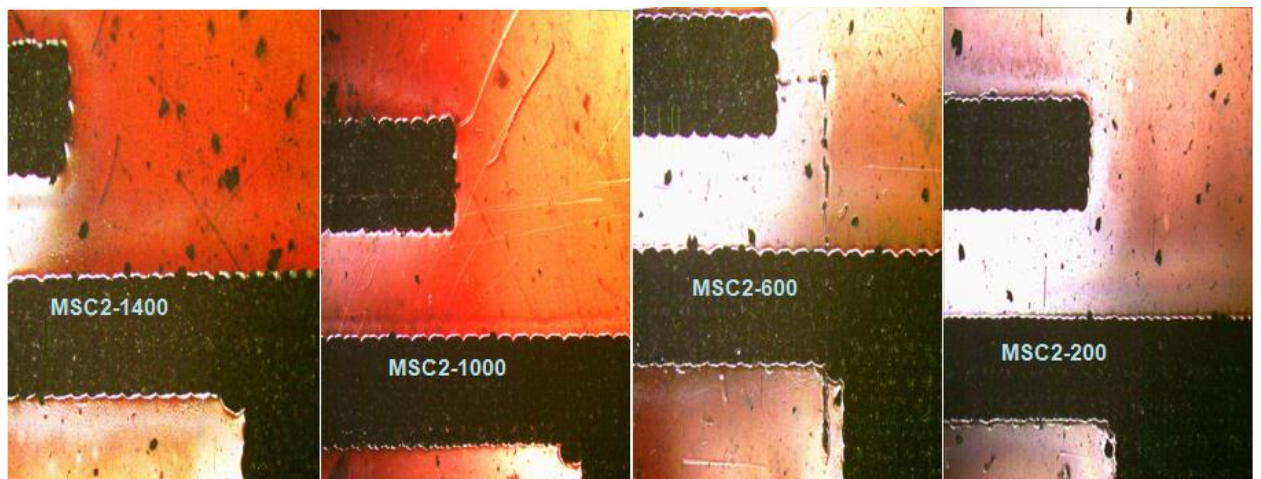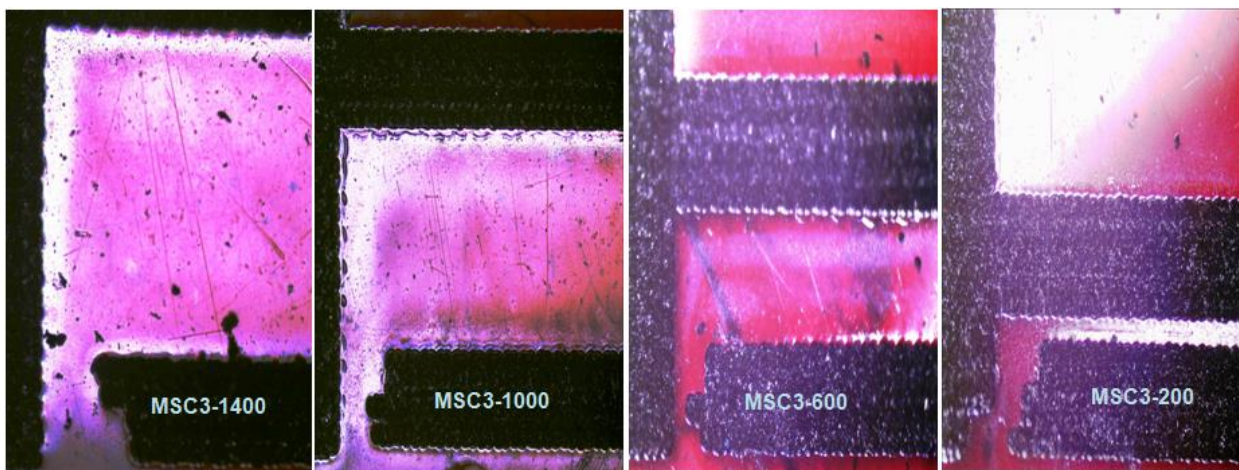

Figure 5.21: Optical Micrographs of MSC3.

5.3.3.1. *Cyclic Voltammetry*

Figure 5.22 and 5.23 show the cyclic voltammogram and increasing trend in capacitance as the distance between the electrodes decreases. As the distance decreases from 600μm to 200μm we observe a sharp increase in capacitance which has been attributed to high electric field between the two electrodes and is elaborated further in section 5.3.3.2.
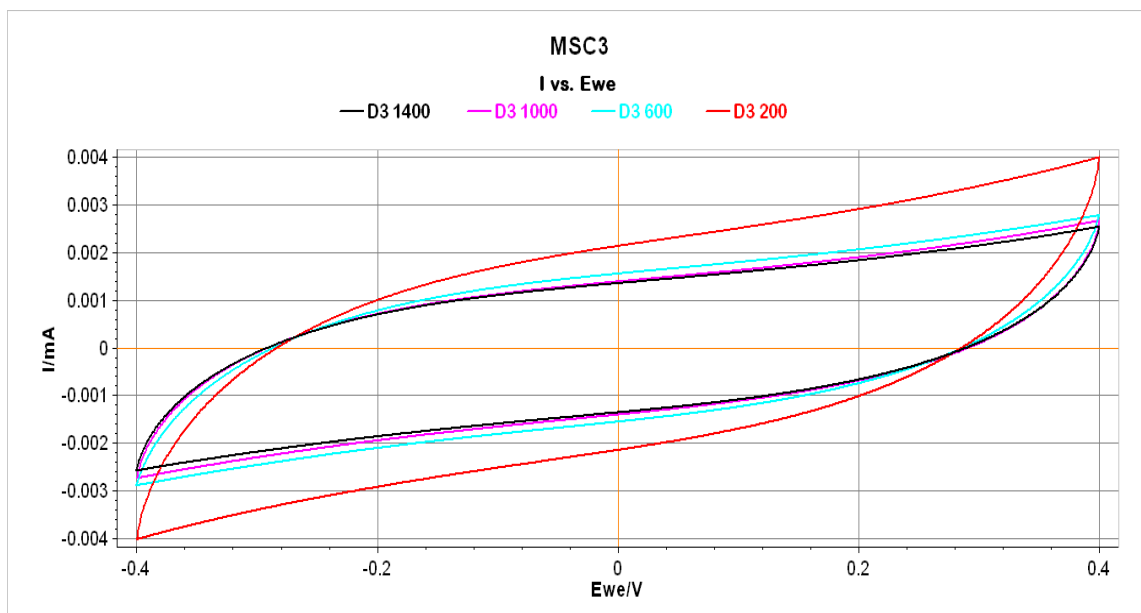
*Figure 5.22: Cyclic Voltammogram for MSC3.*
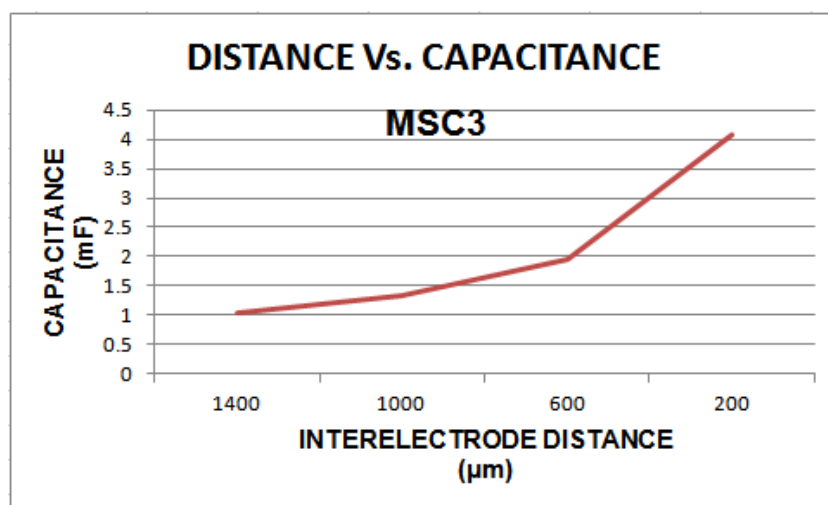
Figure 5.23: Capacitance vs. Interelectrode Distance for MSC3 (Calculated from Cyclic Voltammetry).

5.3.3.2.   *Electrochemical Impedance Spectroscopy*

EIS data and the measured values for MSC3 are shown in figure 5.24 and table 5.5 respectively. As is evident from figure, the value for R_A is significantly smaller for MSC3-200 as compared to other MSC. Similar results were obtained by Kim *et al.* and was attributed to smaller ion diffusion pathway between the electrodes as the distance between them decreased [138]. While this effect is plausible, the increase in R_A and consequently the total capacitance should be somewhat linear as the electrodes move

closer. Instead, as noted by us and Kim *et al.* there is a sharp increase in capacitance as the distance between the electrodes decreases to less than 600μm while for electrode distance greater than 600μm the value of R_A increases by a very small amount (~500Ω for this work). This has led us to suggest that when the electrodes are close together there is a large electric field between them causing electrostatic capacitance between the two and increasing electric double layer capacitance by decreasing the value of R_A. The effect of this electrostatic field decreases drastically when inter-electrode distance is increased beyond 600μm causing a significant decrease in electrostatic capacitance and electric double layer capacitance (due to increased R_A). This effect has also been shown by simulation (section 5.3.3.3). For the design of MSC3 the dominant factor in capacitance decrease is increase in R_A due to sharp decrease in electric field at interelectrode distance greater than 600μm.

The resistance R_{AB} decreases linearly as the distance between electrodes decreases, suggesting that in this case it is dominated by decrease in ion diffusion length rather than by electric field.

k_{BC} also decreases linearly from MSC3-1400 to MSC3-200 and can be explained by the same reasoning as that explained in section 5.3.1.2.
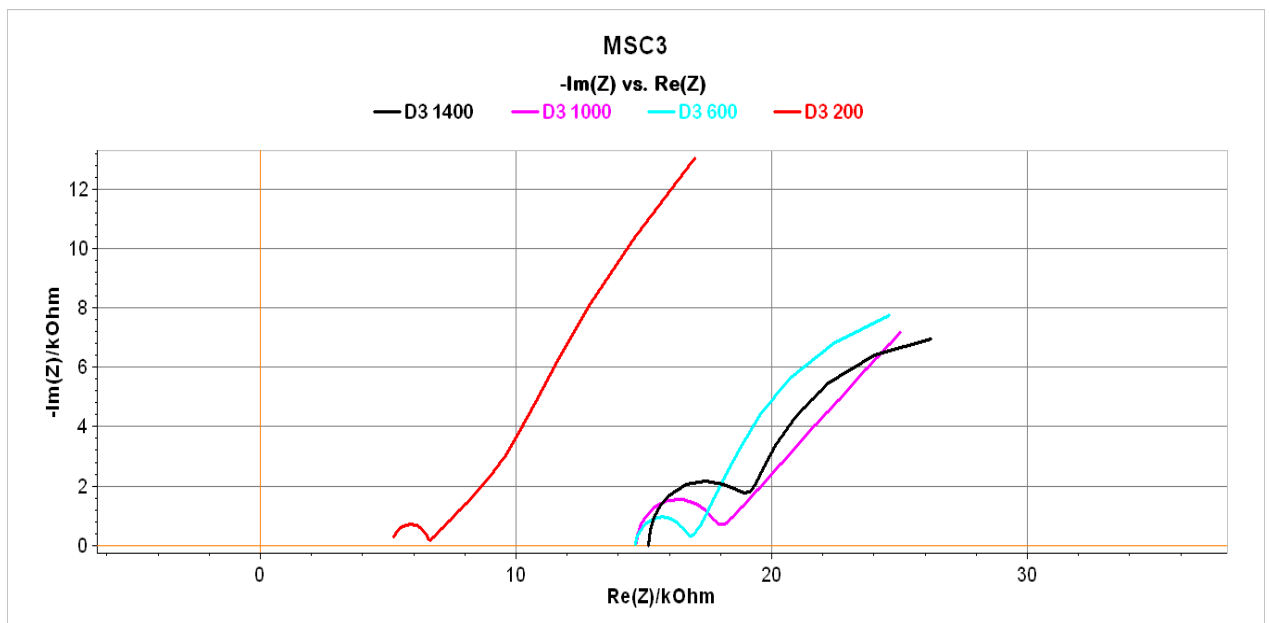
Figure 5.24: Nyquist plot for MSC3.

64

	R_A (KΩ)	R_{AB} (KΩ)	k_{BC}
MSC3-1400	15.18	4.58	0.7508
MSC3-1000	14.68	3.401	0.9481
MSC3-600	14.66	2.192	1.072
MSC3-200	5.141	1.487	1.26

5.3.3.3. Simulation

Figure 5.25 shows the simulation results for MSC3. It is evident from the figure that as the distance between electrodes increases the electric field becomes dispersed and decreases in strength. From figure 5.26 it is seen that at distance less than 600μm there is a sharp increase in electrostatic capacitance due to very high electric field. At the same distance we observe a sharp decrease in R_A (figure 5.24) and an increase in overall capacitance (figure 5.22). At distances greater than 600μm we observe that the electrostatic capacitance between the two electrodes experiences very small decrease and the same effect was observed on R_A and total capacitance obtained from cyclic voltammetry.

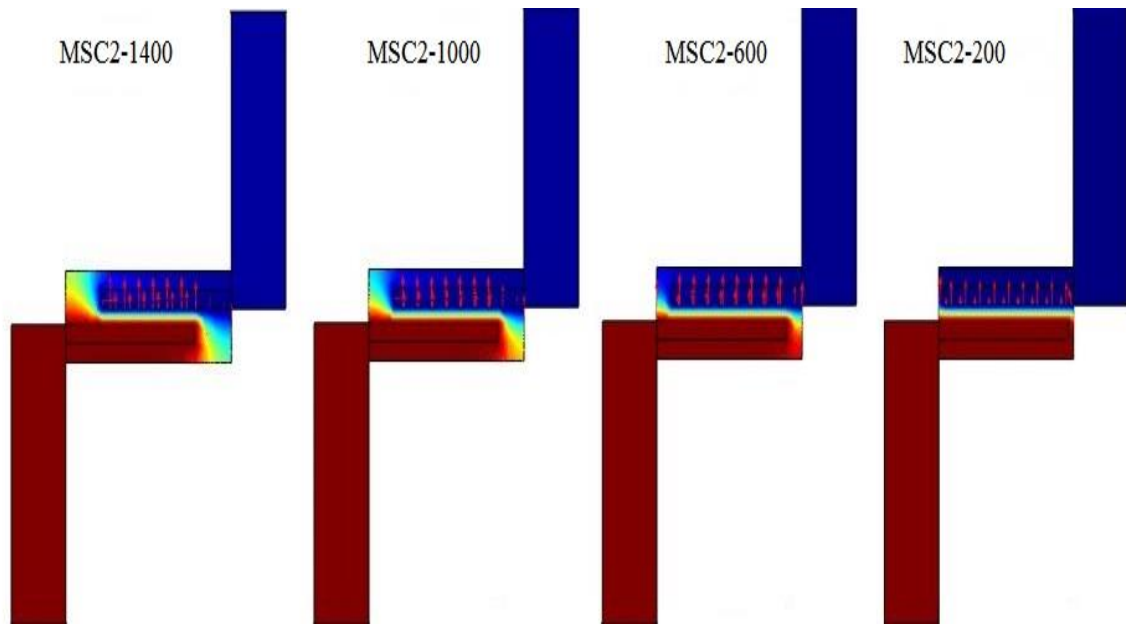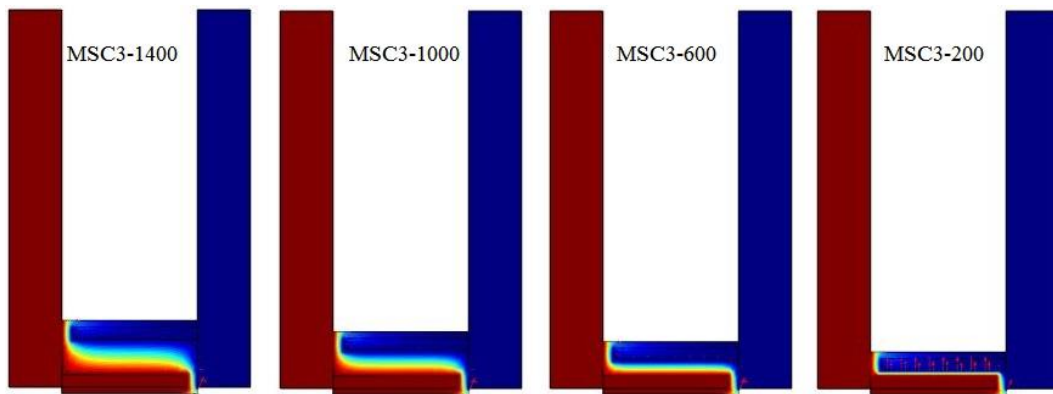*Figure 5.25: Simulation results for MSC3.*

Table 5.6: Electrostatic Capacitance calculated from Simulation of MSC3.

	Capacitance (nF)
MSC3-1400	5.1369
MSC3-1000	5.8006
MSC3-600	7.5573
MSC3-200	17.16
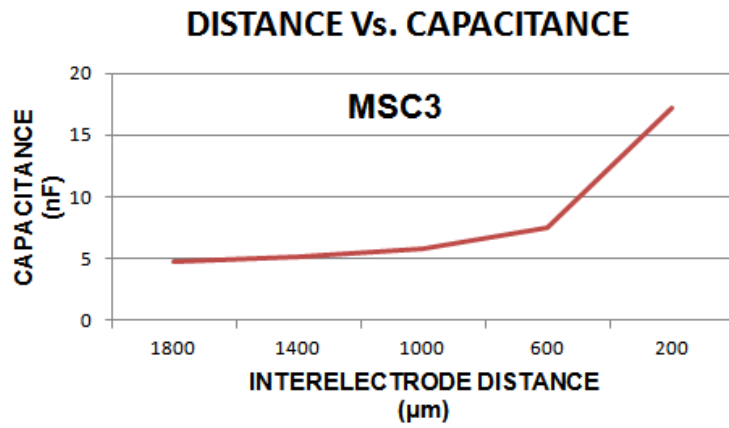
Figure 5.26: Capacitance vs. Interelectrode Distance for MSC3 (Calculated by COMSOL Simulation).

CONCLUSION AND FUTURE RECOMMENDATIONS

CONCLUSION

➢ In this work, laser scribed microsupercapacitors have been fabricated in order to study the effects of design parameters on the total capacitance.

➢ Three different types of MSCs were fabricated, each exploring the effects of different design parameter on the total capacitance and possible causes for any change in capacitance.

➢ It was found that in addition to change in diffusion length of ions, an electric field is produced between parallel electrodes and between electrodes and current collector which adds additional capacitance to the device called electrostatic capacitance and also serves to decrease ion transport resistance into the pore of the electrode.

➢ The electric field decreases sharply between 200-600μm which causes significant decrease in the overall capacitance of the device.

➢ COMSOL Multiphysics was used to verify the existence of electric field between the electrodes and electrode-current collector and calculate electrostatic capacitance between them.

FUTURE RECOMMENDATIONS

➢ In the future, the same principles can be applied to study the effects of design parameters on rigid electric double layer microsupercapacitors and on other EDLC designs such as fractal and nanocoral.

➢ The effect of electric field can also be studied using different electrode and electrolyte materials and the optimal range for maximum electric field strength can be varied using different electrode and electrolyte materials.

➢ In addition, the effect of design parameters can be studied for pseudocapacitors and hybrid capacitors. The effect of electric field between electrodes might change due to redox reactions at the electrode. In the case the electric field strength remains the same as that for EDLC it might be difficult to observe any changes due to significantly high current for pseudocapacitors.

➢ This work can also be used to design more accurate model and equivalent circuit for working of EDLC as the current models presented by Stern and Gouy-Chapman do not provide complete picture of working of EDLC.

REFERENCES

1. Johansson, T.B., et al., *Renewable energy: sources for fuels and electricity*. 1993: Island press.

2. Edenhofer, O., et al., *IPCC special report on renewable energy sources and climate change mitigation.* Prepared By Working Group III of the Intergovernmental Panel on Climate Change, Cambridge University Press, Cambridge, UK, 2011.

3. Glavin, M., et al. *A stand-alone photovoltaic supercapacitor battery hybrid energy storage system*. in *Power Electronics and Motion Control Conference, 2008. EPE-PEMC 2008. 13th*. 2008. IEEE.

4. Glavin, M. and W. Hurley. *Ultracapacitor/battery hybrid for solar energy storage*. in *Universities Power Engineering Conference, 2007. UPEC 2007. 42nd International*. 2007. IEEE.

5. Kularatna, N., K. Milani, and W.H. Round. *Supercapacitor energy storage in solar application: A design approach to minimize a fundamental loss issue by partitioning the load and the storage device*. in *Industrial Electronics (ISIE), 2015 IEEE 24th International Symposium on*. 2015. IEEE.

6. Cabrane, Z., M. Ouassaid, and M. Maaroufi. *Integration of supercapacitor in photovoltaic energy storage: Modelling and control*. in *Renewable and Sustainable Energy Conference (IRSEC), 2014 International*. 2014. IEEE.

7. Zhang, L., et al. *High voltage super-capacitors for energy storage devices applications*. in *Electromagnetic Launch Technology, 2008 14th Symposium on*. 2008. IEEE.

8. Ma, T., H. Yang, and L. Lu, *Development of hybrid battery–supercapacitor energy storage for remote area renewable energy systems.* Applied Energy, 2015. **153**: p. 56-62.

9. Hu, X., K. Tseng, and M. Srinivasan. *Optimization of battery energy storage system with super-capacitor for renewable energy applications*. in *Power Electronics and ECCE Asia (ICPE & ECCE), 2011 IEEE 8th International Conference on*. 2011. IEEE.

10. Burke, A. and H. Zhao. *Applications of supercapacitors in electric and hybrid vehicles*. in *5th European Symposium on Supercapacitor and Hybrid Solutions (ESSCAP), Brasov, Romania*. 2015.

11. Choudhary, N., et al., *High-performance one-body core/shell nanowire supercapacitor enabled by conformal growth of capacitive 2D WS2 layers.* ACS nano, 2016. **10**(12): p. 10726-10735.

12. Jost, K., et al., *Natural fiber welded electrode yarns for knittable textile supercapacitors.* Advanced Energy Materials, 2015. **5**(4): p. 1401286.

13. Michael, S. *The best smart clothing: From biometric shirts to contactless payment jackets*. 2018

14. Olsson, M.I., et al., *Wearable device with input and output structures*. 2016, Google Patents.

15. Ray, K.A., *Flexible solar cell arrays for increased space power.* IEEE Transactions on Aerospace and Electronic Systems, 1967(1): p. 107-115.

16. Crabb, R. and F. Treble, *Thin silicon solar cells for large flexible arrays.* Nature, 1967. **213**(5082): p. 1223.

17. Okaniwa, H., et al. *Production and properties of a-Si: H solar cell on organic polymer film substrate*. in *16th Photovoltaic Specialists Conference*. 1982.

18. OKANIWA, H., et al., *Hydrogenated amorphous silicon solar cell on organic polymer substrate.* IEICE TRANSACTIONS (1976-1990), 1983. **66**(1): p. 34-38.

19. Brody, T.P., *The thin film transistor—A late flowering bloom.* IEEE Transactions on Electron Devices, 1984. **31**(11): p. 1614-1628.

20. Constant A, B.S., Shanks H, Gruber C, Landin A, Schmidt D, Thielen C, Olympie F, and C.J. Schumacher T. *Development of thin film transistor based circuits on flexible polyimide substrates*. in *Proceedings on the Second Symposium on Thin Film Transistors Technologies*. 1994. Miami, Florida: The Electrochemical Society.

21. Theiss, S. and S. Wagner, *Amorphous silicon thin-film transistors on steel foil substrates.* IEEE Electron Device Letters, 1996. **17**(12): p. 578-580.

22. Wong, W.S. and A. Salleo, *Flexible electronics: materials and applications*. Vol. 11. 2009: Springer Science & Business Media.

23. MarketsandMarkets.com. *Flexible Electronics & Circuit Market by Application (OLED & LCD Display, Printed Sensor, Battery, Thin-Film PV, OLED Lighting), Circuit Structure (Single-Sided, Multilayer, Double-Sided, Rigid), Vertical, and Geography - Global Forecast to 2023*. 2018

24. Afentakis, T., et al., *Design and fabrication of high-performance polycrystalline silicon thin-film transistor circuits on flexible steel foils.* IEEE Transactions on Electron Devices, 2006. **53**(4): p. 815-822.

25. Ma, E.Y. and S. Wagner, *Amorphous silicon transistors on ultrathin steel foil substrates.* Applied physics letters, 1999. **74**(18): p. 2661-2662.

26. Plichta, A., A. Weber, and A. Habeck, *Ultra thin flexible glass substrates.* MRS Online Proceedings Library Archive, 2003. **769**.

27. MacDonald, W.A., *Engineered films for display technologies.* Journal of Materials Chemistry, 2004. **14**(1): p. 4-10.

28. Long, K., et al., *Stability of amorphous-silicon TFTs deposited on clear plastic substrates at 250/spl deg/C to 280/spl deg/C.* IEEE Electron Device Letters, 2006. **27**(2): p. 111-113.

29. Dine-Hart, R. and W. Wright, *Preparation and fabrication of aromatic polyimides.* Journal of Applied Polymer Science, 1967. **11**(5): p. 609-627.

30. Kim, B.J. and E. Meng, *Review of polymer MEMS micromachining.* Journal of Micromechanics and Microengineering, 2015. **26**(1): p. 013001.

31. Dyson, R.W., *Specialty polymers*. 1987: Springer.

32. Nagaraj, K., K. Sangeeth, and G. Hegde. *Nanostructure patterning on flexible substrates using electron beam lithography*. in *International Conference on Experimental Mechanics 2013 and Twelfth Asian Conference on Experimental Mechanics*. 2014. International Society for Optics and Photonics.

33. Scholten, K. and E. Meng, *Electron-beam lithography for polymer bioMEMS with submicron features.* Microsystems & Nanoengineering, 2016. **2**: p. 16053.

34. Acikgoz, C., et al., *Polymers in conventional and alternative lithography for the fabrication of nanostructures.* European Polymer Journal, 2011. **47**(11): p. 2033-2052.

35. Engstrom, D.S., et al., *Additive nanomanufacturing–a review.* Journal of Materials Research, 2014. **29**(17): p. 1792-1816.

36. del Campo, A. and E. Arzt, *Fabrication approaches for generating complex micro-and nanopatterns on polymeric surfaces.* Chemical reviews, 2008. **108**(3): p. 911-945.

37. Torres, C.S., et al., *Nanoimprint lithography: an alternative nanofabrication approach.* Materials Science and Engineering: C, 2003. **23**(1-2): p. 23-31.

38.   Wan, Z., et al., *Laser-Reduced Graphene: Synthesis, Properties, and Applications.* Advanced Materials Technologies, 2018. **3**(4): p. 1700315.

39.   Srinivasan, R., et al., *Ultraviolet laser irradiation of the polyimide, PMDA-ODA (Kapton™), to yield a patternable, porous, electrically conducting carbon network.* Synthetic metals, 1994. **66**(3): p. 301-307.

40.   Research, T.M., *Supercapacitor Market (Application - Automotive, Industrial, Energy, Consumer Electronics; Product - Double layer supercapacitor, Pseudocapacitor, Hybrid Capacitor; Type - Supercapacitor Module, Supercapacitor Weldable Cell, Board Mounted Supercapacitor) - Global Industry Analysis, Size, Share, Growth, Trends, and Forecast 2018 - 2026*. 2018. p. 263.

41.   Helmholtz, H.v., *Ueber einige Gesetze der Vertheilung elektrischer Ströme in körperlichen Leitern, mit Anwendung auf die thierisch-elektrischen Versuche (Schluss.).* Annalen der Physik, 1853. **165**(7): p. 353-377.

42.   Becker, H.I., *Low voltage electrolytic capacitor*. 1957, Google Patents.

43.   Endo, M., et al., *High power electric double layer capacitor (EDLC's); from operating principle to pore size control in advanced activated carbons.* Carbon letters, 2001. **1**(3_4): p. 117-128.

44.   Kularatna, N., *Energy Storage Devices for Electronic Systems: Rechargeable Batteries and Supercapacitors*. 2014: Academic Press.

45.   Leite, F.L., et al., *Theoretical models for surface forces and adhesion and their measurement using atomic force microscopy.* International journal of molecular sciences, 2012. **13**(10): p. 12773-12856.

46.   Gouy, M., *Sur la constitution de la charge électrique à la surface d'un électrolyte.* J. Phys. Theor. Appl., 1910. **9**(1): p. 457-468.

47.   Chapman, D.L., *LI. A contribution to the theory of electrocapillarity.* The London, Edinburgh, and Dublin philosophical magazine and journal of science, 1913. **25**(148): p. 475-481.

48.   Sharma, P. and T. Bhatti, *A review on electrochemical double-layer capacitors.* Energy conversion and management, 2010. **51**(12): p. 2901-2912.

49.   Chen, T. and L. Dai, *Flexible supercapacitors based on carbon nanomaterials.* Journal of Materials Chemistry A, 2014. **2**(28): p. 10756-10775.

50.   Wei, L. and G. Yushin, *Nanostructured activated carbons from natural precursors for electrical double layer capacitors.* Nano Energy, 2012. **1**(4): p. 552-565.

51.   Novoselov, K.S., et al., *Electric field effect in atomically thin carbon films.* science, 2004. **306**(5696): p. 666-669.

52.   Miller, J.R., R. Outlaw, and B. Holloway, *Graphene electric double layer capacitor with ultra-high-power performance.* Electrochimica Acta, 2011. **56**(28): p. 10443-10449.

53.   Huang, C.-W., et al., *Significantly enhanced charge conduction in electric double layer capacitors using carbon nanotube-grafted activated carbon electrodes.* Journal of Power Sources, 2008. **183**(1): p. 406-410.

54.   Mastragostino, M., C. Arbizzani, and F. Soavi, *Conducting polymers as electrode materials in supercapacitors.* Solid state ionics, 2002. **148**(3-4): p. 493-498.

55.   Dubal, D.P., et al., *CuO cauliflowers for supercapacitor application: Novel potentiodynamic deposition.* Materials Research Bulletin, 2013. **48**(2): p. 923-928.

56.   Sankapal, B., et al., *Presenting highest supercapacitance for TiO2/MWNTs nanocomposites: Novel method.* Chemical Engineering Journal, 2014. **247**: p. 103-110.

57.   Conway, B., V. Birss, and J. Wojtowicz, *The role and utilization of pseudocapacitance for energy storage by supercapacitors.* Journal of Power Sources, 1997. **66**(1-2): p. 1-14.

58.   Ruiz, V., et al., *Voltage dependence of carbon-based supercapacitors for pseudocapacitance quantification.* Electrochimica Acta, 2013. **95**: p. 225-229.

59.   Gates, B.D., *Flexible electronics.* Science, 2009. **323**(5921): p. 1566-1567.

60.   Kim, S., et al., *Low-power flexible organic light-emitting diode display device.* Advanced Materials, 2011. **23**(31): p. 3511-3516.

61.   Koo, M., et al., *Bendable inorganic thin-film battery for fully flexible electronic systems.* Nano letters, 2012. **12**(9): p. 4810-4816.

62.   Park, S., M. Vosguerichian, and Z. Bao, *A review of fabrication and applications of carbon nanotube film-based flexible electronics.* Nanoscale, 2013. **5**(5): p. 1727-1752.

63.   Shi, S., et al., *Flexible supercapacitors.* Particuology, 2013. **11**(4): p. 371-377.

64.   Yang, Y., et al., *Waterproof, Ultrahigh Areal-Capacitance, Wearable Supercapacitor Fabrics.* Advanced Materials, 2017. **29**(19): p. 1606679.

65.   Akinwolemiwa, B., C. Peng, and G.Z. Chen, *Redox electrolytes in supercapacitors.* Journal of the electrochemical society, 2015. **162**(5): p. A5054-A5059.

66. Deschamps, M., et al., *Exploring electrolyte organization in supercapacitor electrodes with solid-state NMR.* Nature materials, 2013. **12**(4): p. 351.

67. Lu, X., et al., *Flexible solid-state supercapacitors: design, fabrication and applications.* Energy & Environmental Science, 2014. **7**(7): p. 2160-2181.

68. Meng, C., et al., *Highly flexible and all-solid-state paperlike polymer supercapacitors.* Nano letters, 2010. **10**(10): p. 4025-4031.

69. Wang, K., et al., *An All-Solid-State Flexible Micro-supercapacitor on a Chip.* Advanced Energy Materials, 2011. **1**(6): p. 1068-1072.

70. Kang, Y.J., et al., *All-solid-state flexible supercapacitors based on papers coated with carbon nanotubes and ionic-liquid-based gel electrolytes.* Nanotechnology, 2012. **23**(6): p. 065401.

71. Wang, G., et al., *LiCl/PVA gel electrolyte stabilizes vanadium oxide nanowire electrodes for pseudocapacitors.* ACS nano, 2012. **6**(11): p. 10296-10302.

72. Yuan, L., et al., *Flexible solid-state supercapacitors based on carbon nanoparticles/MnO2 nanorods hybrid structure.* ACS nano, 2011. **6**(1): p. 656-661.

73. Choi, B.G., et al., *High performance of a solid-state flexible asymmetric supercapacitor based on graphene films.* Nanoscale, 2012. **4**(16): p. 4983-4988.

74. Xiao, X., et al., *WO3− x/MoO3− x Core/Shell Nanowires on Carbon Fabric as an Anode for All-Solid-State Asymmetric Supercapacitors.* Advanced energy materials, 2012. **2**(11): p. 1328-1332.

75. Cong, H.-P., et al., *Flexible graphene–polyaniline composite paper for high-performance supercapacitor.* Energy & Environmental Science, 2013. **6**(4): p. 1185-1191.

76. Zhu, G., et al., *Highly conductive three-dimensional MnO 2–carbon nanotube–graphene–Ni hybrid foam as a binder-free supercapacitor electrode.* Nanoscale, 2014. **6**(2): p. 1079-1085.

77. Jin, Y., et al., *Graphene-patched CNT/MnO2 nanocomposite papers for the electrode of high-performance flexible asymmetric supercapacitors.* ACS applied materials & interfaces, 2013. **5**(8): p. 3408-3416.

78. Cheng, Y. and J. Liu, *Carbon nanomaterials for flexible energy storage.* Materials Research Letters, 2013. **1**(4): p. 175-192.

79. Lang, J.-W., et al., *Study on the electrochemical properties of cubic ordered mesoporous carbon for supercapacitors.* Journal of Power Sources, 2011. **196**(23): p. 10472-10478.

80.   Liu, W.-w., et al., *Flexible and conductive nanocomposite electrode based on graphene sheets and cotton cloth for supercapacitor.* Journal of Materials Chemistry, 2012. **22**(33): p. 17245-17253.

81.   Niu, Z., et al., *Compact-designed supercapacitors using free-standing single-walled carbon nanotube films.* Energy & Environmental Science, 2011. **4**(4): p. 1440-1446.

82.   Sumboja, A., et al., *Large areal mass, flexible and free-standing reduced graphene oxide/manganese dioxide paper for asymmetric supercapacitor device.* Advanced materials, 2013. **25**(20): p. 2809-2815.

83.   Huang, C.W., et al., *Gel Electrolyte Derived from Poly (ethylene glycol) Blending Poly (acrylonitrile) Applicable to Roll-to-Roll Assembly of Electric Double Layer Capacitors.* Advanced Functional Materials, 2012. **22**(22): p. 4677-4685.

84.   Kang, Y.J., et al., *All-solid-state flexible supercapacitors fabricated with bacterial nanocellulose papers, carbon nanotubes, and triblock-copolymer ion gels.* ACS nano, 2012. **6**(7): p. 6400-6406.

85.   Yu, H., et al., *A novel redox-mediated gel polymer electrolyte for high-performance supercapacitor.* Journal of Power Sources, 2012. **198**: p. 402-407.

86.   Hu, X.-L., et al., *A new nanocomposite polymer electrolyte based on poly (vinyl alcohol) incorporating hypergrafted nano-silica.* Journal of Materials Chemistry, 2012. **22**(36): p. 18961-18967.

87.   Lu, X., et al., *Facile synthesis of large-area manganese oxide nanorod arrays as a high-performance electrochemical supercapacitor.* Energy & Environmental Science, 2011. **4**(8): p. 2915-2921.

88.   Duffy, N., W. Baldsing, and A. Pandolfo, *The nickel–carbon asymmetric supercapacitor—Performance, energy density and electrode mass ratios.* Electrochimica Acta, 2008. **54**(2): p. 535-539.

89.   Prasad, K.R. and N. Miura, *Electrochemical synthesis and characterization of nanostructured tin oxide for electrochemical redox supercapacitors.* Electrochemistry communications, 2004. **6**(8): p. 849-852.

90.   Gupta, V. and N. Miura, *High performance electrochemical supercapacitor from electrochemically synthesized nanostructured polyaniline.* Materials Letters, 2006. **60**(12): p. 1466-1469.

91.   Prasad, K.R. and N. Miura, *Electrochemically synthesized MnO2-based mixed oxides for high performance redox supercapacitors.* Electrochemistry Communications, 2004. **6**(10): p. 1004-1008.

92.   Hu, L., H. Wu, and Y. Cui, *Printed energy storage devices by integration of electrodes and separators into single sheets of paper.* Applied Physics Letters, 2010. **96**(18): p. 183502.

93.   Zheng, G., et al., *Paper supercapacitors by a solvent-free drawing method.* Energy & Environmental Science, 2011. **4**(9): p. 3368-3373.

94.   Hu, L., et al., *Symmetrical MnO2–carbon nanotube–textile nanostructures for wearable pseudocapacitors with high mass loading.* ACS nano, 2011. **5**(11): p. 8904-8913.

95.   Hu, L., et al., *Stretchable, porous, and conductive energy textiles.* Nano letters, 2010. **10**(2): p. 708-714.

96.   Niu, C., et al., *High power electrochemical capacitors based on carbon nanotube electrodes.* Applied Physics Letters, 1997. **70**(11): p. 1480-1482.

97.   Ci, L., et al., *Ultrathick freestanding aligned carbon nanotube films.* Advanced Materials, 2007. **19**(20): p. 3300-3303.

98.   Wang, D., et al., *Highly oriented carbon nanotube papers made of aligned carbon nanotubes.* Nanotechnology, 2008. **19**(7): p. 075609.

99.   Moon, I.K., et al., *Reduced graphene oxide by chemical graphitization.* Nature communications, 2010. **1**: p. 73.

100.   Xin, G., et al., *A graphene sheet exfoliated with microwave irradiation and interlinked by carbon nanotubes for high-performance transparent flexible electrodes.* Nanotechnology, 2010. **21**(40): p. 405201.

101.   Yang, X., et al., *Bioinspired effective prevention of restacking in multilayered graphene films: towards the next generation of high-performance supercapacitors.* Advanced Materials, 2011. **23**(25): p. 2833-2838.

102.   Lu, X., et al., *A flexible graphene/multiwalled carbon nanotube film as a high performance electrode material for supercapacitors.* Electrochimica Acta, 2011. **56**(14): p. 5115-5121.

103.   Strong, V., et al., *Patterning and electronic tuning of laser scribed graphene for flexible all-carbon devices.* ACS nano, 2012. **6**(2): p. 1395-1403.

104.   El-Kady, M.F. and R.B. Kaner, *Scalable fabrication of high-power graphene micro-supercapacitors for flexible and on-chip energy storage.* Nature communications, 2013. **4**: p. ncomms2446.

105.   El-Kady, M.F., et al., *Engineering three-dimensional hybrid supercapacitors and microsupercapacitors for high-performance integrated energy storage.* Proceedings of the National Academy of Sciences, 2015: p. 201420398.

106.   Lu, X., et al., *Hydrogenated TiO2 nanotube arrays for supercapacitors.* Nano letters, 2012. **12**(3): p. 1690-1696.

107.   Luo, Y., et al., *Seed-assisted synthesis of highly ordered TiO 2@ α-Fe 2 O 3 core/shell arrays on carbon textiles for lithium-ion battery applications.* Energy & Environmental Science, 2012. **5**(4): p. 6559-6566.

108.   Bae, J., et al., *Fiber supercapacitors made of nanowire-fiber hybrid structures for wearable/flexible energy storage.* Angewandte Chemie International Edition, 2011. **50**(7): p. 1683-1687.

109.   Wang, Z.-L., et al., *Controllable synthesis of ZnO-based core/shell nanorods and core/shell nanotubes.* RSC Advances, 2011. **1**(1): p. 48-51.

110.   Bao, L., J. Zang, and X. Li, *Flexible Zn2SnO4/MnO2 core/shell nanocable– carbon microfiber hybrid composites for high-performance supercapacitor electrodes.* Nano letters, 2011. **11**(3): p. 1215-1220.

111.   Kim, B., et al., *Preparation and enhanced stability of flexible supercapacitor prepared from Nafion/polyaniline nanofiber.* Synthetic Metals, 2010. **160**(1-2): p. 94-98.

112.   Jin, M., et al., *Flexible electrodes based on polypyrrole/manganese dioxide/polypropylene fibrous membrane composite for supercapacitor.* Electrochimica Acta, 2011. **56**(27): p. 9838-9845.

113.   Duay, J., et al., *Highly flexible pseudocapacitor based on freestanding heterogeneous MnO 2/conductive polymer nanowire arrays.* Physical Chemistry Chemical Physics, 2012. **14**(10): p. 3329-3337.

114.   Lee, Y.-S., et al., *Composite gel polymer electrolytes containing core-shell structured SiO2 (Li+) particles for lithium-ion polymer batteries.* Electrochemistry Communications, 2012. **17**: p. 18-21.

115.   Lu, X., et al., *High energy density asymmetric quasi-solid-state supercapacitor based on porous vanadium nitride nanowire anode.* Nano letters, 2013. **13**(6): p. 2628-2633.

116.   Gao, H. and K. Lian, *High rate all-solid electrochemical capacitors using proton conducting polymer electrolytes.* Journal of Power Sources, 2011. **196**(20): p. 8855-8857.

117.   Gao, H. and K. Lian, *Advanced proton conducting membrane for ultra-high rate solid flexible electrochemical capacitors.* Journal of Materials Chemistry, 2012. **22**(39): p. 21272-21278.

118.   Chen, Q., et al., *Effect of different gel electrolytes on graphene-based solid-state supercapacitors.* RSC Advances, 2014. **4**(68): p. 36253-36256.

119.   Vassal, N., E. Salmon, and J.-F. Fauvarque, *Electrochemical properties of an alkaline solid polymer electrolyte based on P (ECH-co-EO).* Electrochimica Acta, 2000. **45**(8-9): p. 1527-1532.

120.   Lewandowski, A., et al., *Supercapacitor based on activated carbon and polyethylene oxide–KOH–H2O polymer electrolyte.* Electrochimica Acta, 2001. **46**(18): p. 2777-2780.

121.   Yang, C.-C. and S. Lin, *Preparation of alkaline PVA-based polymer electrolytes for Ni–MH and Zn–air batteries.* Journal of applied electrochemistry, 2003. **33**(9): p. 777-784.

122.   Iwakura, C., et al., *New electric double layer capacitor with polymer hydrogel electrolyte.* Electrochemical and solid-state letters, 2003. **6**(2): p. A37-A39.

123.   Yang, C.-C., S.-T. Hsu, and W.-C. Chien, *All solid-state electric double-layer capacitors based on alkaline polyvinyl alcohol polymer electrolytes.* Journal of power sources, 2005. **152**: p. 303-310.

124.   Li, R.-Z., et al., *High-rate in-plane micro-supercapacitors scribed onto photo paper using in situ femtolaser-reduced graphene oxide/Au nanoparticle microelectrodes.* Energy & Environmental Science, 2016. **9**(4): p. 1458-1467.

125.   Feng, J., et al., *Metallic few-layered VS2 ultrathin nanosheets: high two-dimensional conductivity for in-plane supercapacitors.* Journal of the American Chemical Society, 2011. **133**(44): p. 17832-17838.

126.   Choi, B.G., et al., *Facilitated ion transport in all-solid-state flexible supercapacitors.* ACS nano, 2011. **5**(9): p. 7205-7213.

127.   In, J.B., et al., *Facile fabrication of flexible all solid-state micro-supercapacitor by direct laser writing of porous carbon in polyimide.* Carbon, 2015. **83**: p. 144-151.

128.   Gao, W., et al., *Direct laser writing of micro-supercapacitors on hydrated graphite oxide films.* Nature Nanotechnology, 2011. **6**(8): p. 496.

129.   Peng, Z., et al., *Flexible boron-doped laser-induced graphene microsupercapacitors.* ACS nano, 2015. **9**(6): p. 5868-5875.

130.   Liu, Q., M.H. Nayfeh, and S.-T. Yau, *Brushed-on flexible supercapacitor sheets using a nanocomposite of polyaniline and carbon nanotubes.* Journal of Power Sources, 2010. **195**(21): p. 7480-7483.

131.   Jung, H.Y., et al., *Transparent, flexible supercapacitors from nano-engineered carbon films.* Scientific reports, 2012. **2**: p. 773.

132.   Liu, C., et al., *Graphene-based supercapacitor with an ultrahigh energy density.* Nano letters, 2010. **10**(12): p. 4863-4868.

133.   Zhang, K., et al., *Graphene/polyaniline nanofiber composites as supercapacitor electrodes.* Chemistry of Materials, 2010. **22**(4): p. 1392-1401.

134.   Lee, H.Y. and J.B. Goodenough, *Supercapacitor behavior with KCl electrolyte.* Journal of Solid State Chemistry, 1999. **144**(1): p. 220-223.

135.   Zhang, L.L., R. Zhou, and X. Zhao, *Graphene-based materials as supercapacitor electrodes.* Journal of Materials Chemistry, 2010. **20**(29): p. 5983-5992.

136.   Wei, T.Y., et al., *A cost-effective supercapacitor material of ultrahigh specific capacitances: spinel nickel cobaltite aerogels from an epoxide-driven sol–gel process.* Advanced materials, 2010. **22**(3): p. 347-351.

137.   Reddy, A.L.M., et al., *Asymmetric flexible supercapacitor stack.* Nanoscale research letters, 2008. **3**(4): p. 145.

138.   Kim, S.K., et al., *Selective Wetting-Induced Micro-Electrode Patterning for Flexible Micro-Supercapacitors.* Advanced Materials, 2014. **26**(30): p. 5108-5112.

139.   Ferris, A., et al. *Potentialities of micro-supercapacitors as energy storage buffers in embedded micro-systems*. in *Design, Test, Integration and Packaging of MEMS/MOEMS (DTIP), 2016 Symposium on*. 2016. IEEE.

140.   Xie, B., et al., *Laser-processed graphene based micro-supercapacitors for ultrathin, rollable, compact and designable energy storage components.* Nano Energy, 2016. **26**: p. 276-285.

141.   Wang, G., et al., *Wearable supercapacitors on polyethylene terephthalate fabrics with good wash fastness and high flexibility.* Journal of Power Sources, 2017. **367**: p. 34-41.

142.   Li, L., et al., *Flexible planar concentric circular micro-supercapacitor arrays for wearable gas sensing application.* Nano Energy, 2017. **41**: p. 261-268.

143.   Hota, M.K., et al., *Fractal electrochemical microsupercapacitors.* Advanced Electronic Materials, 2017. **3**(10): p. 1700185.

144.   Kazemzadeh, R. and W.S. Kim. *Flexible temperature sensor with laser scribed graphene oxide*. in *Nanotechnology (IEEE-NANO), 2014 IEEE 14th International Conference on*. 2014. IEEE.

145.   Lee, S.-H., J.H. Kim, and J.-R. Yoon, *Laser Scribed Graphene Cathode for Next Generation of High Performance Hybrid Supercapacitors.* Scientific reports, 2018. **8**(1): p. 8179.

146.   El-Kady, M.F., et al., *Laser scribing of high-performance and flexible graphene-based electrochemical capacitors.* Science, 2012. **335**(6074): p. 1326-1330.

147.   Singh, S.P., et al., *Sulfur-Doped Laser-Induced Porous Graphene Derived from Polysulfone-Class Polymers and Membranes.* ACS nano, 2017. **12**(1): p. 289-297.

148.   Yazdi, A.Z., et al., *Direct Creation of Highly Conductive Laser-Induced Graphene Nanocomposites from Polymer Blends.* Macromolecular rapid communications, 2017. **38**(17): p. 1700176.

149.   de Araujo, W.R., et al., *Single-Step Reagentless Laser Scribing Fabrication of Electrochemical Paper-Based Analytical Devices.* Angewandte Chemie, 2017. **129**(47): p. 15309-15313.

150.   Ye, R., et al., *Laser-Induced Graphene Formation on Wood.* Advanced Materials, 2017. **29**(37): p. 1702211.

151.   Chyan, Y., et al., *Laser-Induced Graphene by Multiple Lasing: Toward Electronics on Cloth, Paper, and Food.* ACS nano, 2018. **12**(3): p. 2176-2183.

152.   Lamberti, A., et al., *All-SPEEK flexible supercapacitor exploiting laser-induced graphenization.* 2D Materials, 2017. **4**(3): p. 035012.

153.   Xu, Y., et al., *Alumina sandpaper-supported nickel nanocoatings and its excellent application in non-enzymatic glucose sensing.* Applied Surface Science, 2018.

154.   Li, L., et al., *High-Performance Pseudocapacitive Microsupercapacitors from Laser-Induced Graphene.* Advanced Materials, 2016. **28**(5): p. 838-845.

155.   Tao, L.-Q., et al., *An intelligent artificial throat with sound-sensing ability based on laser induced graphene.* Nature Communications, 2017. **8**: p. 14579.

156.   Tian, H., et al., *Wafer-scale integration of graphene-based electronic, optoelectronic and electroacoustic devices.* Scientific reports, 2014. **4**: p. 3598.

157.   Naveed, S., et al. *A Laser Scribed Graphene Oxide and Polyimide Hybrid Strain Sensor*. in *Key Engineering Materials*. 2018. Trans Tech Publ.

158.   Qiao, Y., et al., *Multilayer Graphene Epidermal Electronic Skin.* ACS nano, 2018.

159.   Lau, N.Y., *Development of Flexible Lithium Sulfur Batteries Based on Laser-Induced Graphene*. 2018, University of Waterloo.

160.   Li, X., et al., *Athermally photoreduced graphene oxides for three-dimensional holographic images.* Nature communications, 2015. **6**: p. 6984.

161.   Lin, J., et al., *Laser-induced porous graphene films from commercial polymers.* Nature communications, 2014. **5**: p. 5714.

162.   Smirnov, V.A., et al., *Photoreduction of graphite oxide.* High Energy Chemistry, 2011. **45**(1): p. 57-61.

163.   Zhang, H. and Y. Miyamoto, *Graphene production by laser shot on graphene oxide: An ab initio prediction.* Physical Review B, 2012. **85**(3): p. 033402.

164.   You, X., et al., *Preparation of an electric double layer capacitor (EDLC) using Miscanthus-derived biocarbon.* ACS Sustainable Chemistry & Engineering, 2017. **6**(1): p. 318-324.

165.   Wu, Z.S., et al., *Graphene-based in-plane micro-supercapacitors with high power and energy densities.* Nature communications, 2013. **4**: p. 2487.

166.   Song, B., et al., *Water-dispersible graphene/polyaniline composites for flexible micro-supercapacitors with high energy densities.* Nano Energy, 2015. **16**: p. 470-478.

167.   Lin, Y., Y. Gao, and Z. Fan, *Printable Fabrication of Nanocoral-Structured Electrodes for High-Performance Flexible and Planar Supercapacitor with Artistic Design.* Advanced Materials, 2017. **29**(43): p. 1701736.

168.   Masarapu, C., et al., *Effect of temperature on the capacitance of carbon nanotube supercapacitors.* ACS nano, 2009. **3**(8): p. 2199-2206.

169.   Stoller, M.D., et al., *Graphene-based ultracapacitors.* Nano letters, 2008. **8**(10): p. 3498-3502.

170.   Wang, S., et al., *High-performance all solid-state micro-supercapacitor based on patterned photoresist-derived porous carbon electrodes and an ionogel electrolyte.* Journal of Materials Chemistry A, 2014. **2**(21): p. 7997-8002.

171.   Lei, C., et al., *Reduction of porous carbon/Al contact resistance for an electric double-layer capacitor (EDLC).* Electrochimica Acta, 2013. **92**: p. 183-187.

172.   Liu, C.-L., et al., *Influence of KOH followed by oxidation pretreatment on the electrochemical performance of phenolic based activated carbon fibers.* Journal of Electroanalytical Chemistry, 2007. **611**(1-2): p. 225-231.

173.   An, K.H., et al., *Electrochemical properties of high-power supercapacitors using single-walled carbon nanotube electrodes.* Advanced functional materials, 2001. **11**(5): p. 387-392.

174.   Nian, Y.-R. and H. Teng, *Influence of surface oxides on the impedance behavior of carbon-based electrochemical capacitors.* Journal of Electroanalytical Chemistry, 2003. **540**: p. 119-127.

175.   Gamby, J., et al., *Studies and characterisations of various activated carbons used for carbon/carbon supercapacitors.* Journal of power sources, 2001. **101**(1): p. 109-116.

176.   Kuphaldt, T.R., *Lessons In Electric Circuits, Volume I–DC*. 2006. p. 439-460.

177.   Heiland, G., *Surface conductivity of semiconductors and its variation by adsorption, transverse electric fields and irradiation.* Discussions of the Faraday Society, 1959. **28**: p. 168-182.

178.   Mei, B.-A., et al., *Physical interpretations of Nyquist plots for EDLC electrodes and devices.* The Journal of Physical Chemistry C, 2017. **122**(1): p. 194-206.

179.   Laity, R.W., *DIFFUSION OF IONS IN AN ELECTRIC FIELD1.* The Journal of Physical Chemistry, 1963. **67**(3): p. 671-676.